Exploit the study of the scenarios for the control of the response of single-degree-of-freedom systems with bumpers

Giulia Stefani [a], Maurizio De Angelis [b,*], Ugo Andreaus [b]

[a] *Italian National Fire and Rescue Service, Department of Firefighters, Public Rescue and Civil Defense, Ministry of Interior, Italy*
[b] *Department of Structural and Geotechnical Engineering, Sapienza University of Rome, Via Eudossiana 18, 00184 Rome, Italy*

ARTICLE INFO

ABSTRACT

In earthquake-prone areas, seismic isolation systems are designed to preserve structural safety and prevent occupants' injury and properties' damage. However, seismically isolated structures can be subject to large displacements relative to the ground under earthquakes, which lead to define two problems, the first problem concerns to excessive displacements, whereas the second problem relates to excessive accelerations that occur when the displacements are limited by an obstacle with high relative stiffness. An arrangement that favors the solution of these problems is an appropriate interposition between the isolated structure and the obstacle of the shock absorbers or bumpers. The aim of this paper is to investigate, via numerical parametric analyses, the possibility to exploit the occurrence of impact in a two-sided vibro-impact isolated single-degree-of-freedom (SDOF) system under harmonic base excitation with beneficial effects. Through the analysis of the response scenarios which can occur varying the obstacles' parameters, that is the width of the gap and the mechanical (stiffness and damping) properties, the target is to reduce both the maximum value of the displacement and of the acceleration of the mass, compared to the free flight condition, without possibly reducing the vibration isolation frequency range. This research path leads to the definition of vibro-impacting control systems and to the free and constrained single and multi-objective optimal design of the control system consisting of the integrated assembly of the isolation system, bumpers and gaps. The main results obtained consist in having (i) found a unique optimality condition, (ii) calculated the dissipated energy and given an energetic interpretation to the optimality condition (iii) built maps, that allow to advance behavior predictions, provide indications on the design and allow to make evaluations of the performance of the vibro-impacting system as a function of the stiffness and damping parameters and of the width of the gap. The stiffness ratio and the damping ratio, which define the mechanical properties of the bumpers, are such that the dimensionless relaxation time is about 1, *(iv) finally* the results are compared to multi-objective optimal design. Ultimately, the advantages of this new isolation system are: (1) provide a physical limit switch to the isolation system in order to limit the maximum displacement of the mass; (2) reduce the effects of amplification dynamics in the resonance zone; (3) reduce the static displacement, all without possibly modifying the dynamic response in the isolation zone.

* Corresponding author.
    E-mail address: maurizio.deangelis@uniroma1.it (M. De Angelis).

1. Introduction

In earthquake-prone areas civil structures can experience exceptional loading conditions that may result in wide undesirable losses and damage. In this context, seismic isolation systems are essentially designed to preserve structural safety and prevent occupants' injury and properties' damage. Seismic isolation is used on different scales, from base isolation, to decoupling a superstructure from its substructure resting on a shaking ground, thus protecting a building or nonbuilding structure's integrity, down to a single room in a building. Floor isolation technology can be an efficient and cost-effective means for providing seismic protection for precision equipment or delicate works of art. The major concept in base isolation is to diminish the fundamental frequency of structural vibration to a value lower than the dominant energy frequencies of earthquake ground motions. However, although seismic isolation reduces the risk of damage to a building, because of greater flexibility, seismically isolated structures are expected to experience large displacements relative to the ground, especially under near-fault (NF) earthquakes. The NF ground motions are characterized by one or more intense long-period velocity and displacement pulses, which lead the isolator to undergo large displacements, and possibly to be seriously damaged by exceeding the limit deformation and hence remaining permanently deformed or rupture can even occur [1]. Therefore, In the event of a strong earthquake, it should be taken into account that the seismically isolated structure can face the risk of the occurrence of colliding with a surrounding retaining wall or other adjacent constructions. Such large displacements are accommodated by providing a sufficient seismic clearance as free space, which will later be referred to as gap, around the isolated structure. There are often limitations in the amount of available clearance in the presence of seismically isolated buildings, particularly in the practice of adaptation and reinforcement of existing constructions, situated in metropolitan zones. Thus, the danger of impact on the surrounding moat walls or adjacent structures during severe earthquakes and the likely consequences of these undesired events are of great importance.

The results from parametric studies that have been conducted in the papers of Komodromos et al. [2], of Polycarpou and Komodromos [3], and of Polycarpou and Komodromos [4] on poundings of a seismically isolated building with adjacent structures during strong earthquakes, demonstrated the detrimental effects of potential poundings on the effectiveness of seismic isolation. In particular, both floor accelerations and inter-story deflections of a seismically isolated building increase because of impact, either with the surrounding moat wall or with adjacent buildings, menacing the vulnerable equipment roomed in the structure and the operation of the structure itself. In more detail, the acceleration response exhibits impulses characterized by large frequency and amplitude, the latter being influenced by impact rigidity, in correspondence of the floors where pounding occurs. Therefore, pounding can cause a very crucial problem that is represented by the existence of high spikes in the acceleration response; this problem is particularly accentuated in the case of vulnerable equipment hosted in the buildings [2,5–9].

The isolation of both base and floor structures is characterized by the two problems of large displacements in the absence of impact against obstacles and of large accelerations in the event of impact against obstacles. For both problems, deformable and dissipative bumpers can be used in order to contain both displacements and accelerations. For this purpose it is advisable to preliminarily carry out a numerical and experimental study of the dynamic response scenarios by using a simplified model with one degree of freedom. Polycarpou and Komodromos [4] investigated, through numerical simulations, the effectiveness of using rubber bumpers, which could be attached at locations where it is likely to have impacts, in order to act as shock-absorbers. For the simulation of the dynamic behavior of such rubber bumpers during impacts, a nonlinear force-based impact model, which takes into account the finite thickness of the rubber bumpers, has been developed. Subsequently, a series of parametric analyses are performed to assess the effect of the gap size, the earthquake characteristics and the thickness, compressive capacity and damping of the bumpers. The stiffness of the moat wall is also parametrically considered during poundings of a seismically isolated building, as another potential mitigation measure for poundings of seismically isolated buildings. Moreover, in the case of industrial and power generation facilities [10], acceleration spikes may influence floor response spectra and thus the response of equipment. Thus, considering practical interventions finalized to obtain the mitigation of the impact effects seems to be a very notable task [4].

The impact – from a harmful phenomenon, to be feared and avoided – becomes a constructive tool – to be predicted and exploited – by optimizing the geometric and mechanical parameters of the bumpers, such as gap, damping and stiffness. The occurrence of impact against the obstacles modifies the response of the isolated system, turning it into a nonlinear vibro-impact system. Vibro-impact systems, even the simplest, exhibit complex nonlinear non-smooth dynamics and a wide variety of phenomena (resonances, instabilities, bifurcations, periodic and quasi-periodic trajectories, and even chaotic regimes) that need to be carefully investigated [11]. There are several scientific works, of both numerical and experimental nature, dealing with the nonlinear response of impacting systems. Extremely rich and complex behaviors were observed by Christopher et al. [12] in a multi-degree of freedom structure impacting a rigid stop. Costa et al. [13] experimentally and numerically explore the complex dynamics of the mass excited impact oscillator presented in Wiercigroch et al. [14]. Several interesting behaviors, including period-doubling route to chaos, period-adding cascade, interior and boundary crisis, complete and incomplete chaotic chattering, and different types of bifurcations, were observed by Gritli and Belghith [15] considering a one-degree-of-freedom impact oscillator with a single rigid constraint. Ing et al. [16] investigated the behavior of a nearly symmetrical piecewise linear oscillator with flexible constrains, which is a modification of a rig originally designed by Wiercigroch and Sin [17] and examined the bifurcation scenarios close to grazing. The effect of potential asymmetry in the gap and/or stiffness was also investigated. The most complex and interesting behaviors were observed for small clearances, larger forcing amplitude, and for values of the frequency ratio below the natural frequency [17]. The fundamental group of impact motions which can occur in the response of a two-degree-of-freedom system with a clearance and subjected to harmonic excitation were studied by Luo et al. [18,19]. Pattern types, occurrence and stability domains and bifurcation characteristics of periodic motions in a two-degree-of-freedom mechanical impact oscillator with a clearance were investigated by

Lyu et al. [20]. Considering single and two degree-of-freedom impact oscillators Yin et al. [21] discussed the phenomena of coexisting attractors and chaotic transitions including crisis.

Some of the above-mentioned behaviors are undesirable as they can cause adverse effects [18]. The study of the behavior of vibro-impact systems, allowing to highlight possible issues associated with the occurrence of impact, is therefore necessary to identify suitable strategies to mitigate and control the response of such systems. Several authors proposed different strategies for the control of unstable orbits, bifurcation, co-existing orbits and chaos based on the study of practical problem involving collisions. By using suitable control strategies or by properly selecting the parameters which characterize the vibro-impact problem, it is possible to guide the behavior of the system, in order to avoid certain scenarios and encourage others, and thus exploit the occurrence of impact with beneficial effects. Wang et al. [22] developed a control scheme, named impulsive control method, to stabilize chaotic motions in a class of vibro-impact systems, which consists in implementing the pulses just when the impact occurs. Lenci and Rega [23] proposed to reduce the region of chaotic response of an inverted pendulum with rigid unilateral constraints subjected to a periodic excitation by suitably adjusting the shape of the excitation. The control of multi-stability in a vibro-impact capsule system driven by a harmonic excitation was addressed by Liu and Páez Chávez [24]. The proposed position feedback controller converts the multi-stable capsule system to a bistable one. A position feedback control method, suitable for dealing with chaos control and coexisting attractors, was applied by Liu et al. [25] for enhancing the desirable forward and backward capsule motion. Basins of attraction were used to investigate the possibility of switching between coexisting attractors by using the proposed control method. Gritli and Belghith [15], and Gritli [26] proposed a state-feedback control law to control chaos exhibited by a SDOF impact mechanical oscillator with a single rigid obstacle. A state-feedback controller was designed by Turki et al. [27,28] to stabilize a 1-DoF, periodically forced, impact mechanical oscillator subject to asymmetric two-sided rigid end-stops. Considering two periodically forced oscillators that can interact via soft impacts, Brzeski et al. [29] showed that with properly selection of the system's parameters, such as the gap between the systems or/and the phase shift of external excitation, it is possible to decrease the number of coexisting solutions via discontinuous coupling. The results of the analysis carried out by Sun et al. [30] showed that by properly designing the dynamic parameters of viscoelastic end-stops, the nonlinear vibration of a SDOF nonlinear suspension system at primary resonance can be effectively suppressed and the jump phenomena can be eliminated for both hardening and softening primary isolators. Furthermore, the end-stop can effectively also attenuate the absolute acceleration response for a hardening primary isolator, while more damping is needed to attenuate that for a softening primary isolator. A two-sided damping constraint control strategy was proposed by Hao et al. [31] to improve the performance of the quasi-zero stiffness (QZS) isolator [32]. The proposed control approach can largely lower the isolation frequency while enhancing the effectiveness of isolation in high frequencies and preventing the severity of end-stop impacts. Based on the analysis of two-parameter bifurcations and basins of attraction, the authors found that the key issue to realize such control objective, is the suppression of period-3 solutions that coexist with the desired period-1 orbits.

To improve the performance of seismic isolation used for the protection of precision equipment, Lu and Lin [33], and Reggio and De Angelis [34] proposed effective mitigation strategies for acceleration-sensitive equipment subjected to earthquake. Lu and Lin [33] proposed a smart isolation system (SIS) that combines an isolation platform with a variable friction device. Reggio and De Angelis [34] proposed an equipment isolation system with nonlinear hysteretic behavior and developed a methodology for the optimal design. Reggio and De Angelis [35] designed a passive equipment isolation system composed of High-Damping Rubber Bearings (HDRB) by adopting a coupled approach in which the supporting structure and the isolated equipment are considered as parts of a combined primary–secondary system and analyzed together.

The papers of Caliò and Marletta [36], Contento and Di Egidio [37], and Sorace and Terenzi [38] deal with the passive control of the vibrations of art objects subjected to base excitations. In [36] the art object is modeled as a rigid block simply supported on a pedestal which is connected to a visco-elastic device in order to obtain a passive control system. In [37] the work of art has been modeled with a non-symmetrical rigid body, sitting on a base that is connected to a visco-elastic device, which represents the passive control system. To prevent the breaking of the isolation device, security stops have been introduced to limit the displacement of the oscillating base to a maximum safety value.

In [18,22], an impulsive control method is applied to stabilize the chaotic motions in a class of vibro-impact systems. The strategy of the control is to implement the pulses just when the impact occurs. The numerical results obtained by Wang et al. [22] indicated that the proposed method could suppress chaos into periodic orbits which are embedded in the chaotic attractor effectively, and also showed that the method is robust even for high levels of multiplicative noise or additive noise. A two-degree-of-freedom impact oscillator is considered by Luo et al. in [18]. The maximum displacement of one of the masses is limited to a threshold value by the symmetrical rigid stops. Impacts between the mass and the stops are described by an instantaneous coefficient of restitution. Chaotic-impact motions are suppressed to minimize the adverse effects by using external driving force, delay feedback and feedback-based method of period pulse.

The performance of structures with respect to earthquake excitation can be improved by the technique of seismic isolation, which has often proved to be an effective tool for earthquake-resistant design. Although floor isolation reduces the risk of damage to a building, because of greater flexibility, it causes a significant drift at the level of isolation. In order to account for large relatively displacements, it is necessary to provide a large seismic clearance as free space around the building. A practical limitation is imposed by this specification on the use of earthquake isolation, because there are often limitations in the amount of clearance available in the presence of seismically isolated buildings, which will later be referred to as gaps, particularly in the practice of adaptation and reinforcement of existing constructions, situated in metropolitan zones. Thus, the danger of impact on the surrounding moat walls or adjacent structures during severe earthquakes and the likely consequences of these undesired events are of great importance [39].

In [40] the authors identified and studied two problems, with reference to the type of elaboration of the results provided by the experiments and to the aims that with such elaboration arise. The first problem concerns the control of excessive displacements.

If the displacements are limited by placing an obstacle, accelerations increase because of impact. The second problem relates to the control of excessive accelerations that occur when the displacements are to be limited by inserting a rigid obstacle or – as in reality – a bumper with very high relative stiffness; with the insertion of more deformable bumpers, it is possible to limit the accelerations, but one pays the price of an increase in displacement. The paper [41] is part of a research work carried out by the authors and inspired by the practical problem of excessive displacements in base isolated structures. The research concerns the numerical and experimental investigation of the response of a vibro-impact single-degree-of-freedom (SDOF) system limited by two-sided deformable and dissipative obstacles (bumpers) under harmonic base excitation [40,42–47]. Most of previous (experimental and theoretical) studies focused on the nonlinear behavior (scenarios, resonances,...) exhibited by the vibro-impact system varying selected parameters [42–47]. In the theoretical–numerical study presented in [41] the authors outlined possible scenarios within the system response. This study guided subsequent experimental laboratory campaigns conducted on a small-scale physical model of the system using the shaking table [42–44]. The study of the scenarios was subsequently resumed and extended, both numerically and experimentally, in [45]. The scenarios observed experimentally were characterized and were reproduced numerically showing a good agreement with the experimental results. Further numerical investigations highlighted the existence of more complex and varied behaviors for gaps smaller than those considered in the experimental tests [45–47]. The experimental and numerical study presented in [40], compared to the others, dealt with vibration control. The authors highlighted the existence of suitable pairs of bumpers and gaps that allow to reach a trade-off between two conflicting objectives, namely control of excessive displacements and control of excessive accelerations. This goal can be achieved combining small gaps with quite deformable bumpers. The work [41] represents a deepening and an extension of the study presented in [40]. The aim is to investigate, through numerical parametric analyses, the effect of the presence of existing, or newly added, obstacles on the response of the system under harmonic base excitation, compared to the free flight condition, that is without obstacles. Compared to previous works by the authors [45–47], in [41] the study of the response scenarios which can occur by varying the bumpers' parameters (i.e., gap, stiffness, and damping, respectively) was directed at vibration control. In particular, the possibility to exploit the occurrence of impact with beneficial effects, by properly selecting the bumpers' parameters, was investigated.

The aim of this paper is to investigate, via numerical parametric analyses, the possibility to exploit the occurrence of impact in a two-sided vibro-impact single-degree-of-freedom (SDOF) system under harmonic base excitation with beneficial effects. Through the analysis of the response scenarios which can occur varying the obstacles' parameters, that is the position and the mechanical (stiffness and damping) properties, the target is to reduce both the peak value of the displacement and of the acceleration of the mass, compared to the free flight condition, without possibly reducing the vibration isolation frequency range. The attention is focused both on the resonance condition and on the frequency range of isolation.

Ultimately, the results of the first part [41] of the research work are being exploited to give indications on how to orient the response according to the desired, albeit conflicting, objectives. In the conclusions of [41] it was observed that, for each value of the dimensionless gap δ_0, inside the range of interest, and for constant bumper damping ratio γ and variable bumper stiffness ratio λ, it is possible to identify a condition preferable to the others at which the envelope of the values of the acceleration in resonance condition shows a minimum. This occurs, regardless of the dimensionless gap, when λ and γ, are such that the dimensionless relaxation time $2\xi\gamma/\lambda$ is about 1, ξ being the system damping factor. This observation allows to reduce the number of parameters which characterize the obstacles and which are to be designed from 3 (δ_0, λ and γ) to 2 (δ_0 and λ), since two of them (λ and γ) are related to each other through the relationship:

$$\frac{\gamma}{\lambda} = \frac{1}{2\xi} \tag{1}$$

The paper is organized as follows. In Section 2 the numerical model and the governing equations are presented; in Section 3 the main results given by constrained optimal design are summarized; the results of the numerical simulations concerning the optimal free design are shown and discussed in Section 4; this discussion is extended to multi-objective optimal design is Section 5; finally, the main conclusions and further development of this study are drawn in Section 6.

2. Model and equations of motion

A suitable numerical model, able to simulate the dynamic behavior of a vibro-impact single-degree-of-freedom SDOF system, is shown in Fig. 1. The system consists of a mass (M, highlighted in green), a damper (D, highlighted in blue), and two-sided unilateral deformable and dissipative bumpers (B, highlighted in red) denoted as right bumper (B_R) and left bumper (B_L) respectively, symmetrically positioned on both sides of the mass, at an initial distance (initial gap) G_{0j} (j = R, L). The damper is modeled by a linear elastic element, with stiffness K, and a linear viscous dashpot, with damping coefficient C, arranged in parallel. The two obstacles are massless and, as the damper, they are modeled by a linear elastic element, with stiffness K_j (j = R, L), and a linear viscous dashpot, with damping coefficient C_j (j = R, L), arranged in parallel. The system is subject to a harmonic base acceleration $A_t(t) = A_G \sin \Omega t$, with amplitude A_G and circular frequency Ω.

During its motion, the mass can be or not in contact with the bumpers. The two conditions will be referred to as contact and free flight phases respectively. The equations that govern the motion of the system can be written in the following form:

$$\begin{cases} M\ddot{u}(t) + C\dot{u}(t) + Ku(t) + F_j(t) \cdot \psi_1\left[G_j(t)\right] \cdot \psi_2\left[F_j(t)\right] = -M A_G \sin \Omega t & \text{(2a)} \\ F_i(t) = 0 & \text{(2b)} \end{cases}$$

where it is assumed that whether j = L then i = R, or whether j = R then i = L. In Eq. (2a) $u(t)$ and $u_j(t)$ (j = R, L) denote the displacements, of the mass and of the two bumpers respectively, relative to the ground and the dot ($\cdot$) denotes differentiation with
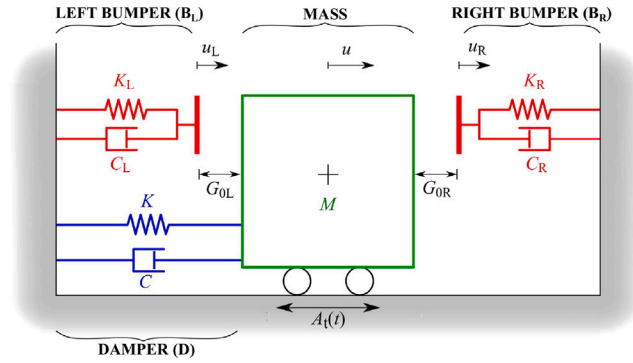
Fig. 1. Model of the SDOF system with two-sided bumpers.

respect to the time t. The absolute acceleration of the mass is given by $a(t) = \ddot{u}(t) + A_t(t)$. $F_j(t) = C_j \dot{u}_j(t) + K_j u_j(t)$ (j = R, L) is the contact force occurring during the contact period with the jth bumper. $G_j(t)$ (j = R, L) is the clearance function which represents the distance, at each time instant, between the mass and the jth bumper:

$$
\begin{cases}
G_j(t) = G_{0j} + \Delta u_j(t) \quad (j = \mathrm{R, L}) & \text{(3a)} \\
\Delta u_R(t) = u_R(t) - u(t) & \\
\Delta u_L(t) = u(t) - u_L(t) & \text{(3b)}
\end{cases}
$$

When the mass is in contact with the jth bumper $G_j(t) = 0$, otherwise $G_j(t) > 0$. Finally, in Eq. (2a), ψ_1 and ψ_2 represent the Heaviside functions, defined as follows:

Approaching contact of the mass to the bumper j : $\psi_1 \left[G_j(t) \right] = \begin{cases} 0, & G_j(t) > 0 \\ 1, & G_j(t) = 0 \end{cases}$ (4a)

Separation of the mass from the bumper j : $\psi_2 \left[F_j(t) \right] = \begin{cases} 0, & F_R(t) \le 0 \text{ or } F_L(t) \ge 0 \\ 1, & F_R(t) > 0 \text{ or } F_L(t) < 0 \end{cases}$ (4b)

Free flight of the mass without contact with any bumper : $\psi_2 \left[F_j(t) \right] = 0$ (j = R, L) (4c)

2.1. Dimensionless equations of motion

The equations of motion of the system (Eqs. (2a)–(2b)) can be written in dimensionless form, by introducing the following characteristic quantities:

$$
\omega = \sqrt{\frac{K}{M}} \tag{5a}
$$

$$
u^* = \frac{M A_G}{K} R_{d,max} = u_{st} R_{d,max} \tag{5b}
$$

$$
F^* = K u^* = M \omega^2 u^* = M A_G R_{d,max} \tag{5c}
$$

namely the natural circular frequency of the SDOF system ω, the maximum relative displacement u^*, the maximum force F^* in the SDOF system in free flight (that is without obstacles) resonance condition. In Eqs. (5b)–(5c) $R_{d,max}(\xi)$ is the maximum value of the dynamic amplification factor $R_d(\xi, \beta)$ – defined as the ratio between the amplitude of the dynamic displacement u to the static displacement $M A_G / K$, at the resonant frequency – which is function of the damping ratio $\xi = C/(2M\omega)$ of the SDOF system, that is $R_{d,max}(\xi) = 1/(2\xi\sqrt{1 - \xi^2})$ for $\xi < \sqrt{2}/2$ (see Appendix A).

By dividing both members of Eqs. (2a)–(2b) by F^* (Eq. (5c)), the equations of motion can be written in the following dimensionless form:

$$
\begin{cases}
q''(\tau) + 2\xi q'(\tau) + q(\tau) + f_j(\tau) \cdot \psi_1 \left[\delta_j(\tau) \right] \cdot \psi_2 \left[f_j(\tau) \right] = -a_G \sin \beta\tau & \text{(6a)} \\
f_i(\tau) = 2\xi\gamma_i q_i'(\tau) + \lambda_i q_i(\tau) = 0 & \text{(6b)}
\end{cases}
$$

where it is assumed that whether j = L then i = R, or whether j = R then i = L. In Eqs. (6a)–(6b) $q = u/u^*$ and $q_i = u_i/u^*$ (i = R, L) are the dimensionless relative displacements of the mass and of the right and left bumper respectively, and the apex ($'$) denotes

differentiation with respect to the dimensionless time $\tau = \omega t$; $a_G = 2\xi\sqrt{1 - \xi^2}$ is the dimensionless amplitude of the base acceleration $a_t(\tau)$; $\beta = \Omega/\omega$ is the ratio between the circular frequency of the base excitation Ω and the natural circular frequency of the SDOF system ω. The normalized absolute acceleration of the mass is therefore given by $\alpha(\tau) = q''(\tau) + a_t(\tau)$. $f_j(\tau) = 2\xi\gamma_j q'_j(\tau) + \lambda_j q_j(\tau)$ $(j = R, L)$ is the normalized contact force occurring during the contact period with the jth bumper; $\lambda_j = K_j/K$ $(j = R, L)$ is the ratio between the stiffnesses of the jth bumper and that of the damper and $\gamma_j = C_j/C$ $(j = R, L)$ is the ratio between the viscous damping coefficients of the jth bumper and that of the damper. The dimensionless clearance function $\delta_j(\tau)$ is defined as follows:

$$
\begin{cases}
\delta_j(\tau) = \delta_{0j} + \Delta q_j(\tau) \quad (j = R, L) & \text{(7a)} \\
\Delta q_R(\tau) = q_R(\tau) - q(\tau) & \\
\Delta q_L(\tau) = q(\tau) - q_L(\tau) & \text{(7b)}
\end{cases}
$$

When the mass is in contact with the jth bumper $\delta_j(\tau) = 0$ $(j = R, L)$, otherwise $\delta_j(\tau) > 0$. In Eq. (7a) $\delta_{0j} = G_{0j}/u^*$ $(j = R, L)$ denotes the initial dimensionless gap between the mass and the jth bumper. Based on the adopted normalization, $\delta_{0j} = 0$ if the jth bumper is initially in contact with the mass; for $0 < \delta_{0j} < 1$ the mass beats and deforms the jth bumper; whereas the mass will be in free flight condition for $\delta_{0j} \geq 1$ $(j = R, L)$, that is the mass is detached from both bumpers. Finally, the Heaviside functions ψ_1 and ψ_2 assume the following expression:

Approaching contact of the mass to the bumper j : $\psi_1\left[\delta_j(\tau)\right] = \begin{cases} 0, & \delta_j(\tau) > 0 \\ 1, & \delta_j(\tau) = 0 \end{cases}$ (8a)

Separation of the mass from the bumper j : $\psi_2\left[f_j(\tau)\right] = \begin{cases} 0, & f_R(\tau) \leq 0 \text{ or } f_L(\tau) \geq 0 \\ 1, & f_R(\tau) > 0 \text{ or } f_L(\tau) < 0 \end{cases}$ (8b)

Free flight of the mass without contact with any bumper : $\psi_2\left[f_j(\tau)\right] = 0$ $(j = R, L)$ (8c)

The particular attention paid to the behavior of the individual bumpers and the assumption of deformable and dissipative bumpers are justified by the fact that the description of both the free flight phase and the contact phase with the mass of the individual bumpers is essential for the purposes of the possibility of achieving the optimization of the system and explaining its mechanical sense.

Despite the relative simplicity of the model, in which both the bumpers and the damper have been modeled with a Kelvin–Voigt model, the system is however strongly nonlinear, due to the presence of clearance, the unilateral constrains and the occurrence of impact that causes abrupt changes of stiffness and damping at the contact time. In this study two equal bumpers symmetrically arranged on the two sides of the mass were considered. Consequently, $\lambda_R = \lambda_L = \lambda$, $\gamma_R = \gamma_L = \gamma$ and $\delta_{0R} = \delta_{0L} = \delta_0$. Furthermore, a step-wise forward and backward sine sweep base acceleration was assumed, that is a harmonic signal with constant amplitude, in which the forcing frequency is increased (forward sweep) and then decreased (backward sweep) over time, within a specific frequency range ($0.05 \leq \beta \leq 3$) and with an appropriate frequency increment ($\Delta\beta = 0.005$), after a certain number (40) of cycles. The equations of motion (Eqs. (2a)–(2b)) were numerically solved using the central difference method [48], implemented with a numerical code written in Matlab. As concerns the identification of the time period in which impact occurs, this was done as follows. The beginning of the contact phase between the mass and the jth bumper was identified based on the value of the clearance function $\delta_j(\tau)$ $(j = R, L)$, as illustrated in Eq. (8a). In particular, impact occurs when $\delta_j(\tau) = 0$. Regarding instead the evaluation of the time instant of detachment, this was made based on the value of the contact force $f_j(\tau)$ $(j = R, L)$, as illustrated in Eq. (8b). This choice was motivated by the necessity to overcome one of the drawbacks of the Kelvin–Voigt model, when used to model the contact, that is the existence of attracting forces after the restitution phase [49–52]. Since this does not make sense from a physical point of view, in this study the change of sign of the contact force was assumed as indicator of the end of the contact phase.

To permit a parametric analysis, one degree-of-freedom (SDOF) systems are studied in this paper. Modeling structures by using SDOF systems imposes a major limitation that the effect of higher vibration modes, which is a major consequence of impact in base-isolated buildings, cannot be included [53,54]. However, the behavior of equipment devices [2], bridge decks [55,56], and buildings representing a very stiff superstructure [54] can be adequately simulated by SDOF models. In all above cases, the maximum acceleration spikes are captured at the base level closest to the point of impact. Furthermore, this is a commonly used in the literature generic model for BIS (see e.g., [57–59]) which renders subsequent numerical results and discussion relevant to different types of structures including stiff low-rise base isolated buildings (e.g., [60]), decks of isolated bridges along their longitudinal direction (e.g. [61]), base isolated storage tanks (e.g., [62,63]), and block-type secondary equipment and artifacts anchored on floor isolation systems within buildings (e.g., [34,35]).

3. From constrained to free optimal design

3.1. Matching mechanism between mass and bumpers

In [41] the constrained optimal design was performed by keeping γ constant and letting λ vary, OPT1, for different values of dimensionless gap δ_0:

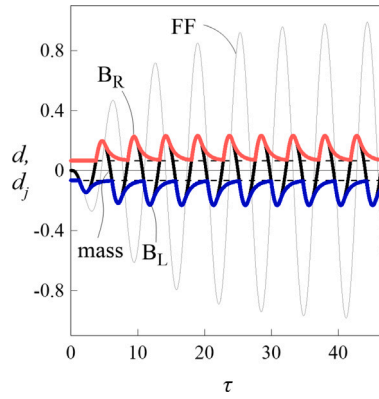$$find_{0.01 \leq \lambda \leq 10} \; minmax\{\eta_a[\lambda|\delta_0\gamma\xi]\}$$ (9a)

Fig. 2. Time histories of the first ten cycles of the response, starting from zero initial conditions, for $\xi = 0.1$, $\gamma = 5$, $\delta_0 \simeq 0.066$, $\lambda = 1$ and $\beta_R \simeq 1.32$: position of the mass d, without (*thin gray line*, free flight — FF) and with (*thick black line*) obstacles, and of the bumpers d_j (j = R, L, *red line* for the right bumper B_R and *blue line* for the left bumper B_L) [41]. (For interpretation of the references to color in this figure legend, the reader is referred to the web version of this article.)

$$subjected\ to\ constraints \begin{cases} 0 \le \delta_0 \le 1 \\ \gamma = constant \\ \xi = 0.1 \end{cases} \tag{9b}$$

where $\eta_a = \Delta\alpha/\Delta\alpha_0$ denotes the maximum excursion $\Delta\alpha$ of absolute acceleration of the mass, normalized with respect to maximum excursion $\Delta\alpha_0$ in the free flight at resonance; The search for optimal parameter values, in this and subsequent optimization problems, was carried out using the Matlab function *fminimax*. In such a way the existence of an optimality condition, corresponding to the minimum value of the maximum absolute acceleration in resonance condition, has been demonstrated, which can be translated into the Eq. (1), which in turn allows to identify an optimal value λ_{opt} for each γ value. In this condition the bumpers have enough time to recover their deformation, after the detachment from the mass, by dissipating energy. Furthermore, they do not remain inactive because impact practically occurs immediately after recovery (Fig. 2).

For completeness of description of the mechanics of the system, we point out the existence of two non-optimality conditions complementary to the optimality condition mentioned above; in the first condition the bumper is hit by the mass when it has not yet recovered all its deformation and therefore has not dissipated all the energy stored during the impact, and in the second condition the bumper is hit by the mass after it has recovered all its deformation and has remained inactive for a more or less long time.

The physical–theoretical mechanism underlying the optimization of the vibro-impacting system is the dissipation of energy by the bumpers and the damper. In fact, Eq. (1) links together the non-dimensional stiffness λ and damping γ of the bumpers to the damping factor ξ of the damper, and constrains the bumpers to be, alternating, always active so as to be able to completely dissipate the elastic energy stored in the bumper springs via the bumper dampers themselves. In this sense, the ratio γ/λ that satisfies Eq. (1) is optimal from the point of view of energy dissipation. In fact, among all the pairs of parameters γ and λ considered in Figs. 4a and b, there is only one that satisfies Eq. (1) and it is the one that minimizes the maximum of η_a and maximizes the maximum energy dissipated by the bumpers, as shown in Figs. B.11a and B.12a reported in Appendix B. For further confirmation of the mechanism physical–theoretical basis of the proposed optimization, it always occurs that although the overall energy dissipated by the bumpers and the damper during the impact phase is always lower than that dissipated by the damper alone in the free flight phase, the dissipation mechanism of energy offered by the bumpers is more effective (in the sense of reducing response) than that offered by the damper.

In [41] it was also observed that in the optimal condition neither jumps nor hysteresis occur, and in addition to the minimum value of the acceleration in resonance condition, also a significant reduction of the displacement was noted. Added to this is also the reduction in static displacement for small gaps.

3.2. Further results

The results presented in [41] are extended in this paper, considering in addition to the constrained optimal design with respect to parameter γ also the constrained optimal design with respect to parameter λ and searching for the minimum of the absolute acceleration η_a, while the displacement has not a minimum. In this case the optimal design conducted for $\lambda = constant$ and γ variable, OPT2, leads to finding the optimal value γ_{opt}:

$$find_{0.01 \le \gamma \le 10}\ minmax\{\eta_a[\gamma|\delta_0\lambda\xi]\} \tag{10a}$$

$$subjected\ to\ constraints \begin{cases} 0 \le \delta_0 \le 1 \\ \lambda = constant \\ \xi = 0.1 \end{cases} \tag{10b}$$

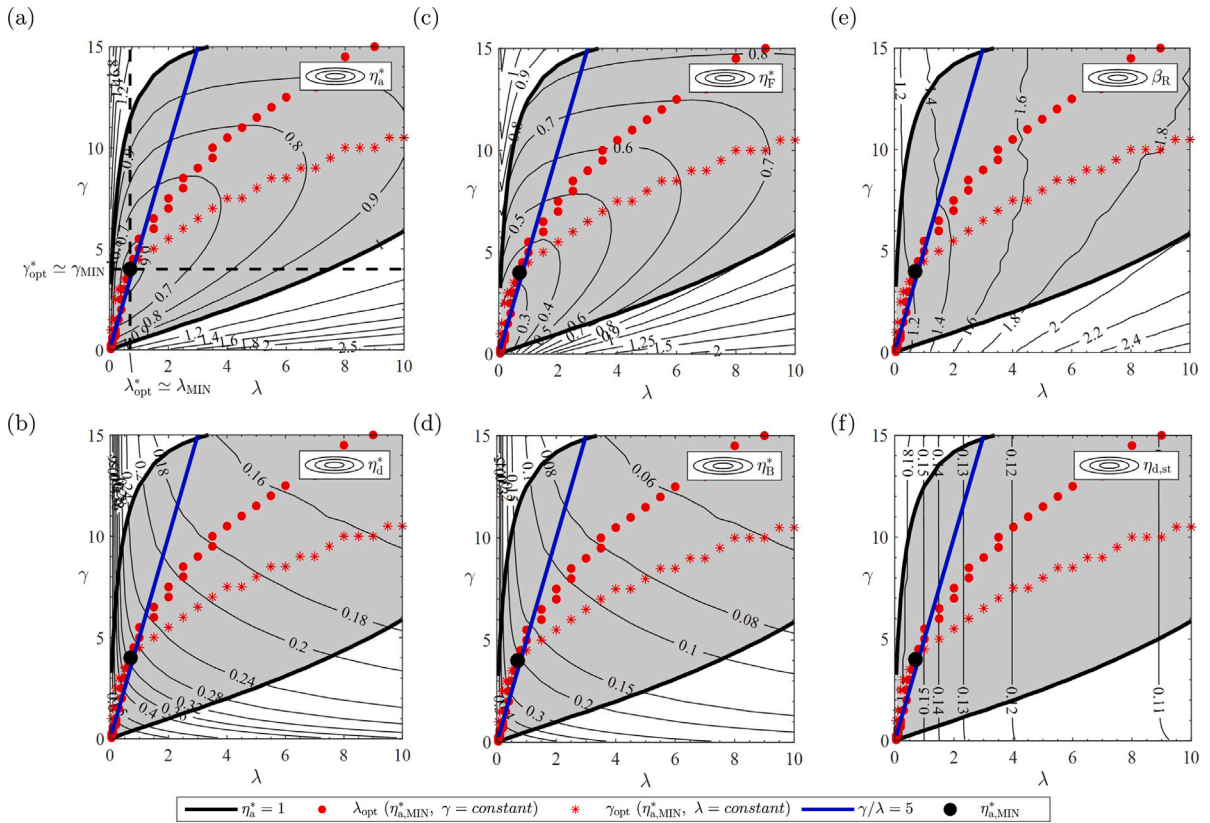**Fig. 3.** Contour maps of: (a) η_a^*; (b) η_d^*; (c) η_F^*; (d) η_B^* for $\xi = 0.1$, $\delta_0 = 0.1$, $0.05 \leq \lambda \leq 10$ and $0.05 \leq \gamma \leq 15$. (For interpretation of the references to color in this figure legend, the reader is referred to the web version of this article.)

Furthermore, free optimal design is also considered, by not imposing any constraints on parameters λ and γ. Now, free optimal design is performed letting both λ and γ vary within suitable ranges for a single value of gap δ_0, OPT3, conducting to the couple values λ_{opt}^* and γ_{opt}^*:

$$find_{0.01 \leq \gamma \leq 10}^{0.01 \leq \lambda \leq 10} \ minmax\{\eta_a[\lambda, \gamma | \delta_0 \xi]\} \tag{11a}$$

$$subjected \ to \ constraints \begin{cases} \delta_0 = constant \\ \xi = 0.1 \end{cases} \tag{11b}$$

Finally, the constraint Eq. (1) has been added to the free optimal design, OPT4; in this case the optimization problem is to find the parameter λ bounded within a predetermined searching range [0.01,10], for any values of δ_0 within the range [0,1], for γ dependent on λ as it is subject to the optimality relationship Eq. (1) and for a fixed value of $\xi = 0.10$. Therefore, this procedure can be expressed mathematically in the form:

$$find_{0.01 \leq \lambda \leq 10} \ minmax\{\eta_a[\lambda | \gamma \delta_0 \xi]\} \tag{12a}$$

$$subjected \ to \ constraints \begin{cases} \gamma = \frac{\lambda}{2\xi} \\ 0 \leq \delta_0 \leq 1 \\ \xi = 0.1 \end{cases} \tag{12b}$$

Fig. 3 shows the results of the different optimal designs previously described: the black curve represent the free flight condition ($\eta_a^* = 1$), red dots represent the constrained optimization, λ_{opt} ($\eta_{a,MIN}^*$, $\gamma = constant$), OPT1, red stars represent the constrained optimization γ_{opt} ($\eta_{a,MIN}^*$, $\lambda = constant$), OPT2, the black dot represents the free optimization, $\eta_{a,MIN}^*$, OPT3, and, blue line represent the optimization constrained by $\gamma / \lambda = 5$, Eq. (1), OPT4.

The considered optimal designs, yet generally conducting the different results, in correspondence with the absolute minimum of the acceleration, converge to a unique couple of optimal values $\lambda_{opt}^* - \gamma_{opt}^*$, Fig. 3a, which satisfies Eq. (1), and depends only on parameters δ_0 and ξ. All this was shown by varying the dimensionless gap with the final result of obtaining an optimality curve in the plane $\lambda - \delta_0$ which reduces the design parameters to just one, i.e. the gap.
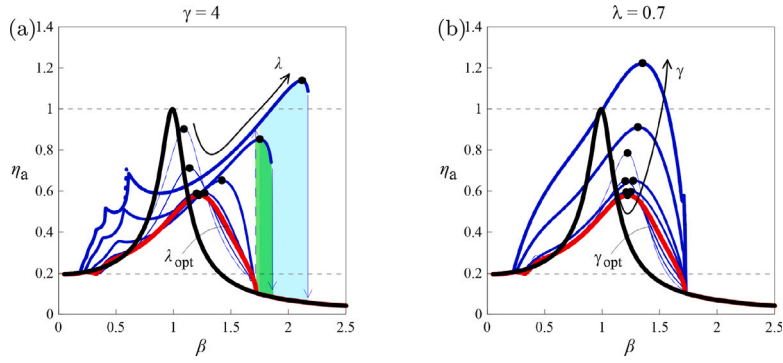
Fig. 4. Sections of the PRCs of η_a for $\xi = 0.1$, $\delta_0 = 0.1$: (a) $\gamma = 4$ and each curve corresponds to a different value of the stiffness ratio λ ($0.1 \leq \lambda \leq 10$); (b) $\lambda = 0.7$ and each curve corresponds to a different value of the damping ratio γ ($1 \leq \gamma \leq 15$). (For interpretation of the references to color in this figure legend, the reader is referred to the web version of this article.)

The selected response quantities are the normalized excursions of absolute acceleration of the mass $\eta_a = \Delta\alpha/\Delta\alpha_0$, relative displacement of the mass $\eta_d = \Delta q/\Delta q_0$, contact force $\eta_F = \Delta f_B/\Delta\alpha_0$ and deformation of the bumpers $\eta_B = \Delta q_B/\Delta q_0$. The excursion was calculated as the difference between the maximum and minimum values recorded at steady state of each sub-frequency range. The excursion of the contact force (Δf_B) and of the bumpers' deformation (Δq_B) were calculated as the sum of the maximum absolute values of the contact forces and of the deformations of the two bumpers respectively, recorded at steady state of each sub-frequency range. The normalization was made with respect to the free flight condition at resonance. $\Delta\alpha_0$ and Δq_0 denote the maximum excursion of the absolute acceleration and of the relative displacement of the mass respectively in free flight resonant condition. In addition to these response quantities, some considerations regarding the resonant frequency β_R of the acceleration and the excursion of the static displacement $\eta_{d,st}$ of the mass will also be made. The values which the response quantities (η_a, η_d, η_F, and η_B) assume at the primary resonance are denoted with a superscript star, namely: η_a^*, η_d^*, η_F^* and η_B^*.

The Figs. 3a-d show, in the $\lambda - \gamma$ plane, the contour maps of the above-mentioned resonant values of the selected response quantities η_i^* (i = a, d, F, B) and the Figs. 3e-f the contour maps of the acceleration resonant frequency β_R and the excursion $\eta_{d,st}$ of the static displacement respectively, for fixed values of the damping factor ($\xi = 0.1$) and of the dimensionless gap ($\delta_0 = 0.1$). The influence of the stiffness and damping ratios, λ and γ, is investigated within the ranges: $0.05 \leq \lambda \leq 10$ and $0.05 \leq \gamma \leq 15$. It can be observed that the contour plot of η_F^* (Fig. 3c) is similar to that of η_a^* (Fig. 3a), whereas the contour plot of η_B^* (Fig. 3d) is similar to that of η_d^* (Fig. 3b). By looking at Fig. 3a it can be observed that there is a region in the $\lambda - \gamma$ plane (highlighted in gray) in which, despite the occurrence of impact, the peak value of the excursion of the absolute acceleration of the mass is lower than in the free flight condition ($\eta_a^* < 1$). The absolute minimum of the acceleration $\eta_{a,MIN}^*$ (represented with a thick black dot), for γ and λ freely varying within the above-mentioned ranges, occurs for $\lambda_{MIN} \simeq 0.7$ and $\gamma_{MIN} \simeq 4$, according to the free optimal design mode; the stiffness and damping ratios corresponding to the absolute minimum of acceleration are such that $\gamma_{MIN}/\lambda_{MIN} \simeq 5$; the values λ_{MIN} and γ_{MIN} give the coordinates of the thick black dot.

Compared to the free flight condition ($\lambda = \gamma = 0$, no obstacles), at the absolute minimum of the acceleration (black dot), a significant reduction (about 70%) of the peak excursion of the relative displacement of the mass is observed (Fig. 3b). Also, the excursion of the static displacement (Fig. 3f) is reduced (about -20%). The resonant frequency of the acceleration is increased (about +23%, Fig. 3e). The condition corresponding to the absolute minimum of the acceleration involves a resonant excursion of the contact force of about 35% (Fig. 3c) and of the bumper's deformation of about 20% (Fig. 3d).

The optimality relationship Eq. (1) is represented in the $\lambda - \gamma$ plane by a straight blue line. It can be noted that this line captures well the minimum value of η_a^* (Fig. 3a). Along the blue line, as λ (or γ) increases, η_a^*, starting from a unit value for $\lambda = \gamma = 0$ (no obstacles), first decreases, reaches a minimum (black dot), and then starts to increase.

For reader's convenience, the shaded gray region where $\eta_a^* < 1$ and the blue line representative of the relationship $\gamma/\lambda \simeq 5$ are represented in all the sub-figures belonging to Fig. 3, as well as red circles and red stars, which represent respectively the optimal values of λ_{opt} and γ_{opt}, that is the values of λ and γ corresponding to the minimum value of η_a^* for $\gamma = constant$ and $\lambda = constant$ respectively (constrained optimal design). It is interesting to note that in the intervals $0 < \lambda < \lambda_{MIN}$ and $0 < \gamma < \gamma_{MIN}$ the tracing of the red circles and red stars approximately coincides with the blue line, then diverging from it and from each other.

Considering the two sections of the contour map of η_a^*, passing both for the minimum (black dot) and highlighted in Fig. 3a with black dashed lines, Fig. 4 is obtained. In particular, Fig. 4a shows the evolution of the PRCs of η_a with the stiffness ratio λ for $\gamma = constant$, while Fig. 4b shows the evolution of the PRCs of η_a with the damping ratio γ for $\lambda = constant$. The thickness of the lines increases with λ and γ respectively. From Fig. 4a it can be observed that the acceleration resonance frequency β_R (β values corresponding to the black dots) increases as γ increases; as concerns the maximum value of the excursion of the acceleration (η_a values corresponding to the black dots), it decreases from $\lambda = 0.1$ to $\lambda = 0.7$, where it attains the minimum value (λ_{opt}, thick red curve), and then returns to increase from $\lambda = 1$ to $\lambda = 10$; in the λ interval from 1 to 10 there are areas of hysteresis (highlighted in green and cyan) and secondary resonances in the low frequency range, which grow as λ increases.
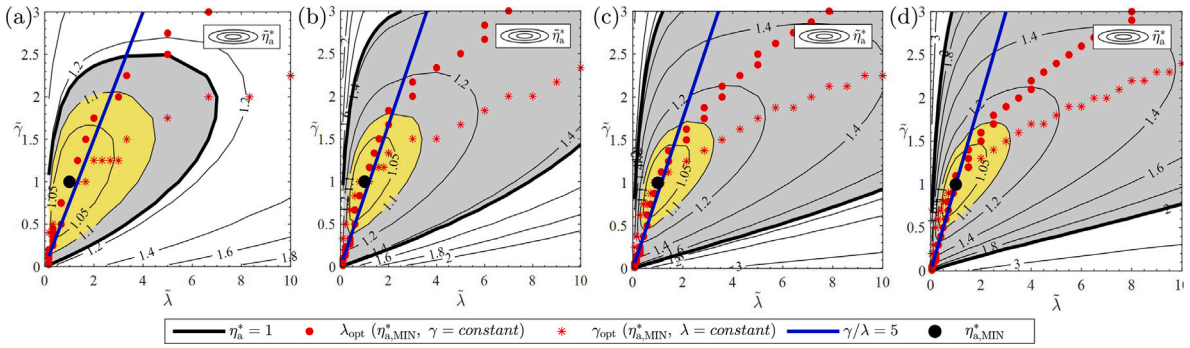
Fig. 5. Contour maps of $\tilde{\eta}_a^* = \eta_a^*/\eta_{a,\mathrm{MIN}}^*$ in the $\tilde{\lambda} - \tilde{\gamma}$ plane (where $\tilde{\lambda} = \lambda/\lambda_{\mathrm{MIN}}$ and $\tilde{\gamma} = \gamma/\gamma_{\mathrm{MIN}}$, with $0.05 \leq \lambda \leq 10$, $0.05 \leq \gamma \leq 15$), for $\xi = 0.1$ and: (a) $\delta_0 = 0.4$; (b) $\delta_0 = 0.2$; (c) $\delta_0 = 0.1$; (d) $\delta_0 = 0.05$. (For interpretation of the references to color in this figure legend, the reader is referred to the web version of this article.)

From Fig. 4b it can be observed that the acceleration resonance frequency β_R (β values corresponding to the black dots) increases with increasing γ; as concerns the maximum value of the excursion of the acceleration (η_a values corresponding to the black dots), it decreases from $\gamma = 1$ to $\gamma = 4$, where it attains the minimum value (γ_{opt}, thick red curve), and then returns to increase from $\gamma = 5$ to $\gamma = 15$; no hysteresis or secondary resonances are observed, at least in the range considered for γ ($1 \leq \gamma \leq 15$) and for the fixed value of $\lambda = 0.7$.

The absolute acceleration η_a can also be interpreted as a transmissibility (TR), because it allows evaluating the ability of the vibro-impacting system to reduce the vibrations through the additional damping associated to the impact between mass and bumpers. In fact, as an example, Fig. 4a shows that two frequency ranges can be identified from the transmissibility η_a black curve, that represent the free flight condition. These ranges are separated by the value $\beta = \sqrt{2}$, which together with $\beta = 0$ identify the two fixed points where transmissibility η_a takes a unity value, i.e., acceleration excursion $\Delta\alpha$ is equal to acceleration excursion $\Delta\alpha_0$ in free fly condition:

- $0 \leq \beta \leq \sqrt{2}$ non-isolation (amplification) range, where transmissibility ηa is greater than or at most equal to 1;
- $\beta > \sqrt{2}$ isolation range, where transmissibility ηa is less than 1.

All the other curves with varying λ present in Fig. 4a and with varying γ present in Fig. 4b represent the transmissibility η_a in the event that the impact occurs and show the influence of the presence of the bumpers compared to free flight.

We now proceed to extend the discussion to other (discrete) values of the dimensionless gap δ_0. Fig. 5 shows the contour maps of normalized peak excursion of the acceleration, denoted as $\tilde{\eta}_a^*$, in the plane of normalized stiffness and damping parameters, denoted as $\tilde{\lambda}$ and $\tilde{\gamma}$ respectively, for $\xi = 0.1$ and for different values of nondimensional gap, namely $\delta_0 = 0.4$ (Fig. 5a), $\delta_0 = 0.2$ (Fig. 5b), $\delta_0 = 0.1$ (Fig. 5c), $\delta_0 = 0.05$ (Fig. 5d). The normalization of η_a^* was made with respect to its own minimum value $\eta_{a,\mathrm{MIN}}^*$, that is $\tilde{\eta}_a^* = \eta_a^*/\eta_{a,\mathrm{MIN}}^*$. The stiffness and damping ratios were normalized with respect to their values corresponding to $\eta_{a,\mathrm{MIN}}^*$, that is $\tilde{\lambda} = \lambda/\lambda_{\mathrm{MIN}}$ and $\tilde{\gamma} = \gamma/\gamma_{\mathrm{MIN}}$, with λ varying in the range $0.05 \leq \lambda \leq 10$ and γ varying in the range $0.05 \leq \gamma \leq 15$.

In Fig. 5 the gray area, the blue solid line, the black dot, the red circles and stars retain the same meaning they have in Fig. 3. As illustrated in [41], Eq. (1), represented with the blue line, is valid for each δ_0 value, with $0 \leq \delta_0 < 1$.

From Fig. 5, it can be observed that the region where the acceleration reduces, compared to the free flight condition, increases as δ_0 decreases (the gray area expands). Conventionally assuming, by way of example, a deviation of 10% from the minimum acceleration value, it can also be observed that the extension of the region where $\tilde{\eta}_a^* < 1.1$, highlighted in yellow, and, thus, the robustness of the system, approximately decreases with a decrease of δ_0.

In the next section the discussion will be generalized by moving continuously along the blue line representative of Eq. (1) shown in Figs. 3 and 5, within a continuous range of values of the dimensionless gap δ_0, performing the so-called optimization constrained by the optimality condition Eq. (1).

4. Results

4.1. Optimal design under optimality condition

We now proceed with the optimal design that satisfies the optimality relationship (Eq. (1)), considering the δ_0 parameter that varies between 0 and 1, and evaluating the optimal values of parameter λ, and thus of γ, which corresponds to the absolute minimum of the peak excursion of the absolute acceleration (in the following denoted as λ_{opt}^* and γ_{opt}^* respectively), and which turn to approximately coincide with the coordinates of the thick black dot in Fig. 3.

The discussion will be generalized by moving continuously along the blue line representative of the optimality condition Eq. (1), shown in Figs. 3 and 5. For each δ_0 value, theoretically there would be infinite $\lambda - \gamma$ pairs that satisfy the Eq. (1). It would therefore be interesting to understand if, among these pairs, there is one preferable to the others. To this purpose, in Fig. 6 the evolution of
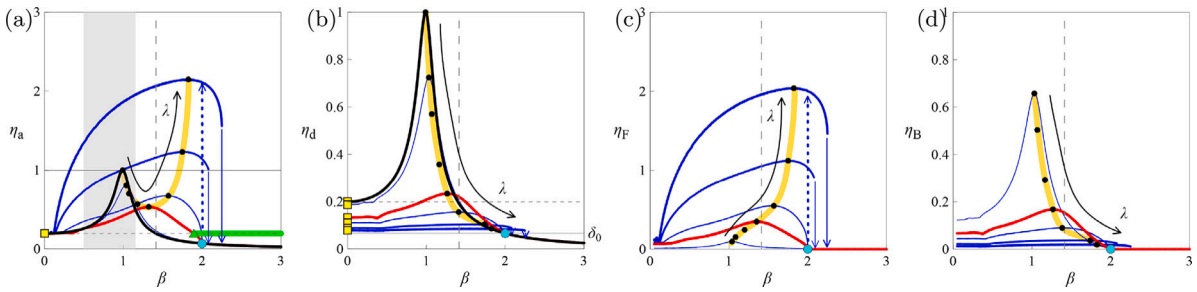
Fig. 6. Sections of the PRCs for $\xi = 0.1$, $\gamma/\lambda = 5$, $\delta_0 \simeq 0.066$ (value of δ_0 so that $\beta_2 = 2$) and for several values of the stiffness ratio λ ($0 < \lambda \leq 10$): (a) η_a; (b) η_d; (c) η_F; (d) η_B. The *black curves* (in (a) and (b)) represent the free flight condition, the *red curves* identify the PRCs corresponding to the λ value at which the envelope of the maximum values of the acceleration shows a minimum ($\lambda = \lambda^*_{opt}$), while the *blue curves* represent the PRCs corresponding to the other values of λ (the thickness of the lines increases with λ). The *black dots* identify the primary resonance condition. In (a) and (b) the *yellow squares* indicate the values of η_a and η_d for $\beta = 0$. The *cyan circles* represent the location of β_2. Finally, in (a) the *green triangle* identifies the β_c value, for $\lambda = \lambda^*_{opt}$, such that $\eta_a < \eta_a|_{\beta=0}$ for $\beta > \beta_c$ (*horizontal green line*). The *vertical gray band* in (a) highlights the frequency interval in which the PRC of η_a corresponding to $\lambda = \lambda^*_{opt}$ (*red curve*) is below the PRC corresponding to the free flight condition (*black curve*). (For interpretation of the references to color in this figure legend, the reader is referred to the web version of this article.)

the PRCs of the selected response quantities with λ ($0 < \lambda \leq 10$) is illustrated, as an example, for $\delta_0 \simeq 0.066$, $\xi = 0.1$ and $\gamma/\lambda = 5$ (the latter obtained from Eq. (1) by setting $\xi = 0.1$); the value $\delta_0 \simeq 0.066$ of the dimensionless gap corresponds to $\beta_2 = 2$ (Appendix A).

Figs. 6a-d represent the PRCs of η_a, η_d, η_F, η_B respectively. The black curves in Figs. 6a and 6b represent the free flight condition, the red curves identify the PRCs corresponding to the $\lambda - \gamma$ pair at which the envelope of the maximum values of the acceleration shows a minimum ($\lambda = \lambda^*_{opt}$) under the optimality relationship $\gamma = \lambda/(2\xi) = 5$, while the blue curves represent the PRCs corresponding to several $\lambda - \gamma$ pairs, namely: (0.1, 0.5), (1, 5), (2, 10), (5, 25) and (10, 50). The thickness of the line increases with λ. The black dots identify the primary resonance condition. In Figs. 6a and 6b the yellow squares indicate the values of η_a and η_d, for $\beta = 0$, denoted as $\eta_a|_{\beta=0}$ and $\eta_d|_{\beta=0}$ respectively. The cyan circles represent the location of β_2, that is the upper bound of the frequency range where the impact surely occurs due to geometric reasons (see Fig. A.10). Finally, in Fig. 6a the green triangle identifies the β_c value, for $\lambda = \lambda^*_{opt}$, such that $\eta_a < \eta_a|_{\beta=0}$ for $\beta > \beta_c$ (horizontal green line), i.e. the value of β such that the maximum absolute acceleration η_a of the mass is lower than the ground acceleration $\eta_a|_{\beta=0}$. The vertical gray band in Fig. 6a highlights the frequency interval in which the PRC of η_a corresponding to $\lambda = \lambda^*_{opt}$ (red curve) is below the PRC corresponding to the free flight condition (black curve).

It can be observed that, although each PRC shown in Fig. 6 corresponds to a $\lambda - \gamma$ pair that satisfies the relationship $\gamma/\lambda = 5$, the response of the system can vary significantly changing the values of λ and γ individually.

As concerns the trend of the maximum values of the response, highlighted with black dots, the following considerations apply. The resonant frequency increases with λ (and thus with γ) and then, for large values of λ and γ, it remains almost constant ($\beta_R \simeq 1.8$). For small values of the peak value of the acceleration of the mass (Fig. 6a) first decreases, reaches a minimum (lower than one) and then starts to increase again, reaching values greater than one. The peak values of both the displacement of the mass (Fig. 6b) and of the deformation of the bumpers (Fig. 6d) decrease as λ (and thus γ) increases. As concerns the peak value of the contact force, it increases with λ, and thus with γ (Fig. 6c). The static displacement of the mass (yellow squares in Fig. 6b) decreases with λ (and thus with γ).

It is possible to identify a value of λ (denoted as λ_H), beyond which the jump phenomena, and thus the hysteresis, occurs; herein this threshold value is $\lambda_H \simeq 2.6$ for $\delta_0 \simeq 0.066$. Furthermore, denoting as $\delta_{0c} \simeq 0.1915$ the value of the dimensionless gap at which $\beta_2 = \sqrt{2}$, since δ_0 ($\simeq 0.066$) $< \delta_{0c}$ ($\simeq 0.1915$) the introduction of the obstacles modifies, regardless of λ, the response of the system also in the frequency range $\beta > \sqrt{2}$ and the reduction of the isolation frequency interval, compared to the linear case, increases as λ increases.

It is worth noting that, although each PRC shown in Fig. 6 corresponds to a $\lambda - \gamma$ pair which satisfies the relationship $\gamma/\lambda = 5$, it is possible to identify a pair which can be considered preferable to the others. This is the $\lambda - \gamma$ pair at which the peak value of the acceleration shows a minimum, that is $\lambda^*_{opt} \simeq 1$ and $\gamma^*_{opt} \simeq 5$ (thick red curves in Fig. 6a). In this situation, in addition to the reduction of the peak acceleration, which is also lower than the free flight condition ($\eta^*_a < 1$), also a significant reduction of the peak value of both the displacement of the mass and of the static displacement, was observed. Furthermore, the acceleration becomes lower than that of the ground for $\beta > \beta_c \simeq 1.9$ (green triangle in Fig. 6a). At the minimum of acceleration there is a change of the slope in the envelope of the maximum displacements (black dots in Fig. 6b). By observing the envelopes of the maximum values, if the stiffness ratio undergoes a further increase, the displacement is reduced to a lesser extent. On the other hand, significant increases in both the acceleration (Fig. 6a) and the contact force (Fig. 6c) are exhibited.

In Fig. 7 the comparison between three of the considered pairs is made in terms of force–displacement cycles at steady state resonance condition, referring to the mass (Fig. 7a) and to the bumpers (Fig. 7b) respectively. In addition to the gray curve, which in Fig. 7a represents the free flight condition, the blue, red, black curves refer to the $\lambda - \gamma$ pairs (0.5, 2.5), (1, 5) and (2, 10) respectively. For $\lambda = \lambda^*_{opt} = 1$ and $\gamma = \gamma^*_{opt} = 5$ (red curve), the maximum inertia force (and thus the maximum absolute acceleration of the mass), shows a minimum, while the maximum contact force does not show a minimum.
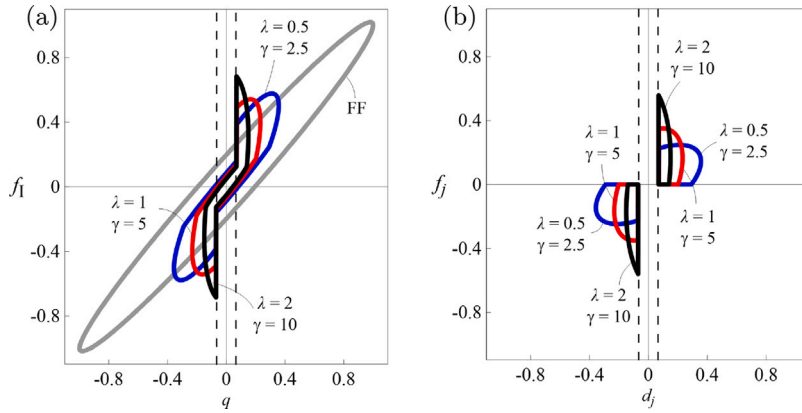
Fig. 7. Force–displacement cycles ($\xi = 0.1$, $\gamma/\lambda = 5$, $\delta_0 \simeq 0.066$) in steady-state resonance condition ($\beta = \beta_R(\lambda)$), without obstacles (free flight FF, $\beta_R \simeq 0.99$, *gray line*), and for $\lambda = 0.5$, $\gamma = 2.5$ ($\beta_R \simeq 1.17$, *blue line*), $\lambda = 1$, $\gamma = 5$ ($\beta_R \simeq 1.32$, *red line*) and $\lambda = 2$, $\gamma = 10$ ($\beta_R \simeq 1.57$, *black line*): (a) mass; (b) bumpers. (For interpretation of the references to color in this figure legend, the reader is referred to the web version of this article.)

By repeating the analysis also for other values of δ_0, in the range $0 \leq \delta_0 < 1$ and for $0 < \lambda \leq 10$, always assuming $\xi = 0.1$ and $\gamma/\lambda = 5$, the contour maps shown in Fig. 8 were obtained. In Figs. 8a-d the contour maps of the peak values of the absolute acceleration of the mass (η_a^*), the relative displacement of the mass (η_d^*), the contact force (η_F^*) and the deformation of the bumpers (η_B^*), respectively, are represented. Figs. 8e and f, instead, show the contour maps of the acceleration resonant frequency β_R and of the excursion of the static displacement $\eta_{d,st}$ respectively.

The contour level corresponding to $\eta_a^* = 1$ is highlighted in Fig. 8a with a thick black line. It can be observed that, in most cases ($\lambda - \delta_0$ pairs), the occurrence of the impact against the obstacle causes an increase of the peak value of the acceleration compared to the free flight condition ($\eta_a^* > 1$); for large values of λ (and thus of γ), η_a^* can reach values up to 2.5. However, for small values of λ (< 10) and for $\delta_0 < 0.8$ the peak value of the acceleration, despite the occurrence of impact, can be lower than in free flight condition ($\eta_a^* < 1$). For each δ_0 value in the range $0 \leq \delta_0 < 0.8$, it is possible to identify the $\lambda - \gamma$ pair corresponding to the minimum peak value of the acceleration under the optimality condition Eq. (1), by performing the so-called optimization constrained by optimality condition. The locus $\lambda_{opt}^*(\delta_0)$ of the λ values corresponding to this condition is represented with a thick dashed red curve; on the other hand, $\gamma = \lambda/(2\xi) = 5$ is given by the optimality condition. It can be observed that the minimum occurs for gradually smaller values of λ as δ_0 increases. For $\delta_0 \geq 0.8$, instead, the peak value of the acceleration is always greater than in free flight condition ($\eta_a^* > 1$) and it increases with λ.

The thick blue line represents the locus of the values of λ, denoted as λ_H, beyond which, for a given δ_0 value, the jump phenomena, and thus the hysteresis, occur. It can be observed that while in the two limit cases ($\delta_0 = 1$ and $\delta_0 = 0$), the hysteresis never occurs, for $0 < \delta_0 < 1$ instead, λ_H decreases as δ_0 decreases, reaching the lower values ($\lambda_H \simeq 1$) for $0.3 < \delta_0 < 0.5$, then it starts to increase again as δ_0 further decreases. It can be noted that, for each δ_0 value, $\lambda_{opt}^* < \lambda_H$, meaning that in the condition corresponding to the minimum peak value of the acceleration of the mass, the hysteresis never occurs.

Finally, the thick green curve represents the locus of the values of λ, delimited by a lower bound value λ_c, beyond which, for a given δ_0 value, the occurrence of impact causes a modification of the system response, compared to the free flight condition, also for $\beta > \sqrt{2}$. It can be observed that this curve tends to an asymptotic value as λ increases. For $\delta_0 \geq$ (about) 0.3, since there are no intersections between the green curve and the horizontal line corresponding to a constant gap ($\lambda_c > \lambda_{max} = 100$), the response will be modified, due to the occurrence of impact, only in the frequency range $\beta < \sqrt{2}$. On the contrary, for $\delta_0 < \delta_{0c} \simeq 0.1915$ the response will be modified also for $\beta > \sqrt{2}$ regardless of λ. For $\delta_{0c} \leq \delta_0 \leq$ (about) 0.3, the isolation frequency range will be modified, compared to the free flight condition, only if $\lambda > \lambda_c$ (on the right of the green curve). The gap range in which the isolation frequency interval is not modified, compared to the linear case (absence of intersections between the green curve and the horizontal line $\delta_0 = constant$), has significantly expanded.

As far as the meaning of the shaded regions is concerned: $\eta_a^* < 1$ in the light gray zone between the black curve and the axis; no hysteresis in the light blue zone to the left of the blue curve; no erosion of the isolation frequency range $\beta > \sqrt{2}$ in the light green zone above the green curve. The black diagonal hatch highlights the region of the $\lambda - \delta_0$ plane in which the three shaded areas overlap. The above-mentioned curves corresponding to $\eta_a^* = 1$ (black curve), λ_{opt}^* (red curve), λ_H (blue curve) and λ_c (green curve) and shaded regions were reported in all the other contour maps (Figs. 8b-f).

As concerns the peak value of the excursion of the relative displacement of the mass (Fig. 8b), it is always lower than in the free flight condition ($\eta_d^* < 1$). It decreases as δ_0 decreases, for a given λ value, and decreases as λ increases, for a given δ_0 value. In the latter case, the extent of the reduction decreases as λ increases (the contour lines tend to become horizontal).

From Fig. 8c it can be observed that the peak value of the excursion of the contact force η_F^* increases with λ, for a given δ_0 value. For a given value of λ, for example $\lambda = 2$, as δ_0 decreases, η_F^* increases, reaches a maximum and then starts to decrease.

As concerns the peak value of the excursion of deformation of the bumpers (Fig. 8d), it decreases with λ, for a given δ_0 value, becoming particularly small for large values of the stiffness ratio. For a given value of λ, for example $\lambda = 2$, as δ_0 decreases, η_B^*
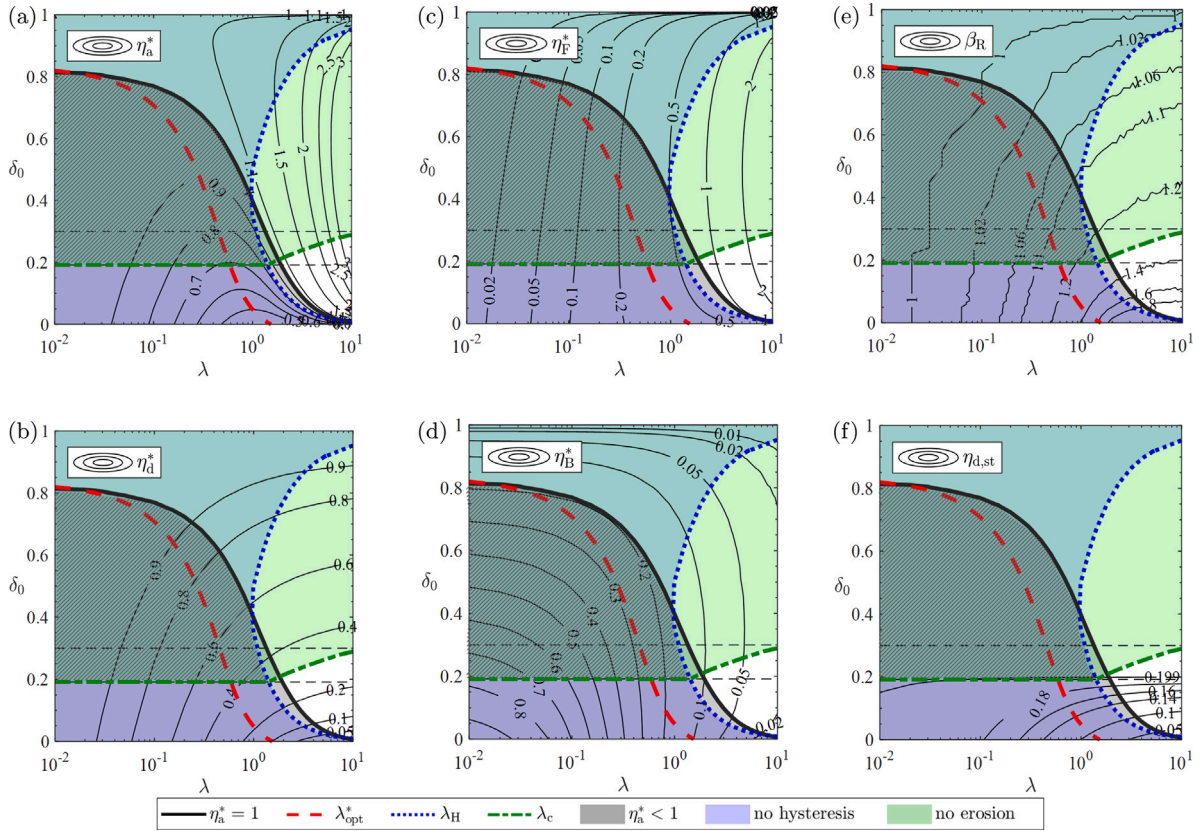
Fig. 8. Contour maps of: (a) η_a^*; (b) η_d^*; (c) η_F^*; (d) η_B^*; (e) β_R; (f) $\eta_{d,st}$ for $\xi = 0.1$, $\gamma/\lambda = 5$, $0.01 \le \lambda \le 10$ and $0 \le \delta_0 \le 1$. The *solid black curve* highlights the contour level corresponding to a unit value of η_a^*. The *dashed red*, *dotted blue* and *dash-dotted green curves* represent the values of λ_{opt}^*, λ_H and λ_c respectively, for each δ_0 value. Meaning of the shaded regions: *light gray*: $\eta_a^* < 1$ (between the *solid black curve* and the λ axis); *light blue*: no hysteresis (to the left of the *dotted blue curve*); *light green*: no erosion of the isolation frequency range $\beta > \sqrt{2}$ (above the *dash-dotted green curve*). The *black diagonal hatch* highlights the region of the $\lambda - \delta_0$ plane in which the three shaded areas overlap. (For interpretation of the references to color in this figure legend, the reader is referred to the web version of this article.)

increases, reaches a maximum and then starts to decrease. For smaller values of λ, for example $\lambda = 0.1$, as δ_0 decreases, η_F^* remains approximately constant, while η_B^* exhibit a positive gradient.

As concerns the resonant frequency (Fig. 8e) it varies between 0.99 and about 3, and the greater values are reached for quite small dimensionless gaps. It increases with λ, for a given δ_0, and it increases as δ_0 decreases, for a given λ value.

Finally, regarding the excursion of the static displacement of the mass, Fig. 8f shows that for $0 \le \delta_0 < 1$ it remains equal to 0.199 independently of δ_0 and λ, whereas for $0 \le \delta_0 < \delta_0^*$ the static displacement decreases as δ_0 decreases, for a given λ value, and as λ increases, for a given δ_0 value. In the latter case, the extent of the reduction decreases as λ increases (the contour lines tend to become almost horizontal).

Ultimately and in summary, the maps shown in Fig. 8 can be assigned the value of design maps, which allow you to choose the optimal value of a selected quantity while also evaluating the loss achieved on the other quantities with respect to their optimal value.

5. Multi-objective optimization

The optimal design that satisfies the optimality relation – minimum of the absolute acceleration (in the following denoted with the suffix (A)) – is compared with the multi-objective optimum that takes into account both acceleration and displacement at the same time (in the following denoted with the suffix (MO)).

From the point of view of a performance approach to the structural impact problem, displacements should also be taken into consideration in addition to accelerations. From an ideal point of view, the simultaneous occurrence of both small accelerations and small displacements would be desirable, since these are conflicting objectives. In this way, equal performance dignity is attributed to displacements and accelerations.
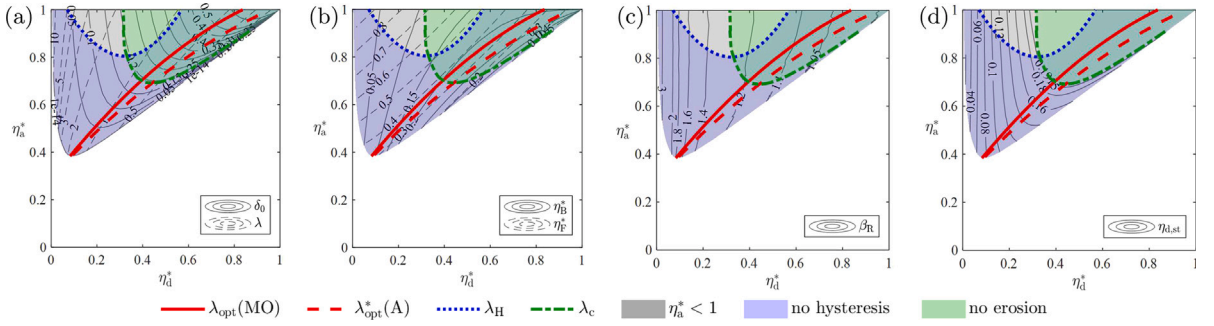
Fig. 9. Contour maps of: (a) δ_0 (*black solid curves*) and λ (*black dashed curves*); (b) η_B^* (*black solid curves*) and η_F^* (*black dashed curves*); (c) β_R (*black solid curves*); (d) $\eta_{d,st}$ (*black solid curves*) for $\xi = 0.1$, $\gamma/\lambda = 5$, $0 \leq \eta_d^* \leq 1$ and $0 \leq \eta_a^* \leq 1$. The *dashed red* and the *solid red curves* represent the locus of the $\eta_d^* - \eta_a^*$ pairs corresponding to the optimal λ values (minimum of the absolute acceleration and multi-objective optimal design respectively), for each δ_0 value. The *dotted blue* and *dash-dotted green curves* represent the $\eta_d^* - \eta_a^*$ pairs corresponding to the λ_H and λ_c values. Meaning of the shaded regions: *light gray*: $\eta_a^* < 1$; *light blue*: no hysteresis; *light green*: no erosion of the isolation frequency range $\beta > \sqrt{2}$. (For interpretation of the references to color in this figure legend, the reader is referred to the web version of this article.)

The objective functions to be minimized as conflicting objectives are the absolute acceleration η_a and the relative displacement η_d of the mass, weighted with the weights w_a and w_d respectively, which in the present work have both been assumed equal to one. The multi-objectives optimization problem is to find the parameter λ bounded within a predetermined searching range [0.01,10], for any values of δ_0 within the range [0,1], for γ dependent on λ as it is subject to the optimality relationship Eq. (1) and for a fixed value of $\xi = 0.10$. Therefore, in this case the procedure can be expressed mathematically in the form:

$$find_{0.01 \leq \lambda \leq 10} \; minmax\{\eta_a, \eta_d[\lambda | w_a, w_d; \gamma, \delta_0, \xi]\} \tag{13a}$$

$$subjected\ to\ constraints \begin{cases} \gamma = \frac{\lambda}{2\xi} \\ 0 \leq \delta_0 \leq 1 \\ \xi = 0.1 \end{cases} \tag{13b}$$

For $\xi = 0.1$ and $\gamma/\lambda = 5$, Fig. 9 shows, in the plane $0 \leq \eta_d^* \leq 1$ and $0 \leq \eta_a^* \leq 1$, the contour maps of: (a) δ_0 (black solid curves) and λ (black dashed curves); (b) η_B^* (black solid curves) and η_F^* (black dashed curves); (c) β_R (black solid curves); (d) $\eta_{d,st}$ (black solid curves). In all the four sub-figures, the colored regions retain the same meaning they have in Fig. 8. In more detail, inequality $\eta_a^* < 1$ is checked within the gray area; no hysteresis occurs in the light blue-colored area; the green color was used to connote the area where no erosion of the isolation frequency range ($\beta > \sqrt{2}$) occurs; the three colored zones are represented in each of the sub-figures a-d of Fig. 9 for comparison's sake.

The blue dotted and the green dash-dotted curves represent the locus of the $\eta_d^* - \eta_a^*$ pairs corresponding to the previously defined λ_H and λ_c values respectively. The red dashed curve represents the locus of the $\eta_d^* - \eta_a^*$ pairs corresponding to the λ value associated with the minimum of the absolute acceleration of the mass (denoted as $\lambda_{opt}^*(A)$), while the solid red curve represents the locus of the $\eta_d^* - \eta_a^*$ pairs corresponding to the optimal λ value obtained with the multi-objective optimization (denoted as $\lambda_{opt}^*(MO)$).

The solid red curve passes through the points of maximum curvature of the contour lines of δ_0 in the performance plane $\eta_d^* - \eta_a^*$ of Fig. 9a. In this way we obtain the points that have the least distance from the origin, which is the ideal case.

Wanting to make a comparison between $\lambda_{opt}^*(A)$ and $\lambda_{opt}^*(MO)$, it can be observed that the two red curves are not so far apart. Indeed, by minimizing acceleration the containment of the displacement is indirectly obtained also. Thus, the optimal design can also be achieved considering the acceleration alone, because the envelope of the acceleration minima (red dashed line) is almost coincident with the envelope of the points of maximum curvature of the δ_0 contour map (red solid line).

6. Conclusions

The aim of this paper is to investigate, via numerical parametric analyses, the possibility to exploit the occurrence of impact in a two-sided vibro-impact SDOF system under harmonic base excitation with beneficial effects. Through the analysis of the response scenarios which can occur varying the obstacles' parameters, that is the width of the gap and the mechanical (stiffness and damping) properties, the target is to reduce the maximum values of both displacement and acceleration of the mass in the impact phase, compared to the free flight condition, without possibly reducing the vibration isolation frequency range.

This research path leads to the definition of vibro-impact control systems and to the free and constrained optimal design of the control system consisting of the integrated assembly of the system, bumpers and gaps.

The main results obtained consist in:

- carrying out a single-objective optimization both free and constrained that minimizes the absolute acceleration of the mass, η_a. The important conclusion is that the considered optimal designs, although generally leading to different results, in correspondence with the absolute minimum of the acceleration, converge to a unique couple of optimal values $\lambda^*_{opt} - \gamma^*_{opt}$, that satisfies Eq. (1), and depends only on parameter δ_0 and ξ. All this was shown by varying the dimensionless gap with the final result of obtaining an optimality curve in the plane $\lambda - \delta_0$ which reduces the design parameters to just one, i.e., the gap.

- having built maps, that allow to advance behavior predictions, provide indications on the design, and allow to make evaluations of the performance of the vibro-impacting system as a function of bumpers' stiffness and damping parameters and of the width of the gap. The stiffness ratio and the damping ratio, which define the mechanical properties of the bumpers, are such that the dimensionless relaxation time is about 1.

- evaluating the energy dissipated by the bumpers and the damper, and observing that: (i) the results obtained confirm the correspondence between the optimal designs and the matching mechanism illustrated in Section 3 also evaluating of the dissipated energy; (ii) in the optimal situation the energy dissipated by the bumpers is maximized; (iii) although the overall energy dissipated by the bumpers and the damper during the impact phase is always lower than that dissipated by the damper alone in the free flight phase, the energy dissipation mechanism offered by the bumpers is more effective (in the sense of reducing the response) compared to that offered by the damper.

- carrying out a multi-objective optimization that simultaneously minimizes both the absolute acceleration and the relative displacement of the mass (conflicting objectives). Furthermore, the two single-objective and multi-objective optimizations were compared, verifying that they lead to approximately the same result.

Ultimately, the advantages of this new isolation system are: (1) provide a physical limit switch to the isolation system in order to limit the maximum displacement of the mass; (2) reduce the effects of dynamics amplification in the resonance zone; (3) reduce the static displacement, all without possibly modifying the dynamic response in the isolation zone.

The possible applications of the results obtained in the engineering field concern all those cases in which collisions with adjacent structures can occur due to excessive displacements, such as isolation systems of structures, buildings and bridges, or equipment, rolling of ships against one or two barrier sides, friction impact of the rotor casing system (drilling systems), normal and inverted pendulums, pipes conveying fluids with end-restraints, nuclear reactors and heat exchangers, and so on.

CRediT authorship contribution statement

Giulia Stefani: Data curation, Formal analysis, Investigation, Software, Visualization, Writing – original draft, Writing – review & editing. **Maurizio De Angelis:** Conceptualization, Funding acquisition, Methodology, Supervision, Validation, Writing – original draft, Writing – review & editing. **Ugo Andreaus:** Conceptualization, Funding acquisition, Methodology, Supervision, Validation, Writing – original draft, Writing – review & editing.

Data availability

No data was used for the research described in the article.

Acknowledgments

Declaration of competing interest

The Authors wish to confirm that there has been no significant financial support for this work that could have influenced its outcome.

Appendix A. Influence of the involved parameters on the system response without and with obstacles

In the absence of obstacles (free flight condition), the response of a viscously damped SDOF system excited by a harmonic base acceleration is influenced by the forcing frequency and the damping. The effect of these parameters on the absolute acceleration and relative displacement response of the system can be seen by observing the trend of the curves of the transmissibility and of the displacement response factor as a function of the frequency ratio and for several values of the damping factor ξ.

In this study, consistently with the normalization adopted in the governing equations (Section 2), both the transmissibility and the displacement response factor were redefined, compared to the classical definition [64]. In both cases, the normalization was made with respect to the maximum response in resonance condition. The analytical expressions of the transmissibility and of the displacement response factor so defined, and denoted as $TR(\xi, \beta)$ and $R(\xi, \beta)$ respectively, are reported in the following Table A.1.

In presence of obstacles, for a given value of the dimensionless gap δ_0, it is possible to preliminary identify the frequency interval in which impact surely will occur, based on geometric considerations, as illustrated in [41]. The limits of this frequency interval,

Table A.1

Analytical expressions related to the transmissibility (left column) and the displacement response factor (right column) for a viscously damped SDOF system excited by a harmonic force.

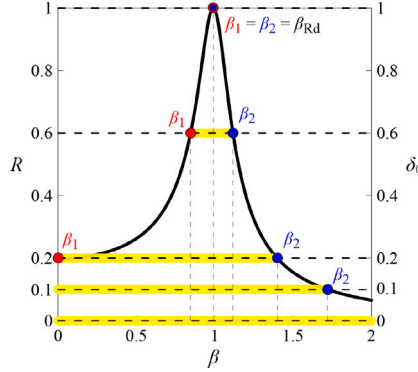| Transmissibility	Displacement response factor
$TR(\xi,\beta) = \dfrac{1}{2\sqrt{2}\xi^2}\sqrt{\dfrac{\left[1+(2\xi\beta)^2\right]\left(-1-4\xi^2+8\xi^4+\sqrt{1+8\xi^2}\right)}{\left(1-\beta^2\right)^2+(2\xi\beta)^2}}$	$R(\xi,\beta) = \dfrac{2\xi\sqrt{1-\xi^2}}{\sqrt{\left(1-\beta^2\right)^2+(2\xi\beta)^2}}$
$TR(\xi,0) = \dfrac{\sqrt{-1-4\xi^2+8\xi^4+\sqrt{1+8\xi^2}}}{2\sqrt{2}\xi^2} = \dfrac{1}{TR_{\mathrm{a,max}}(\xi)}$	$R(\xi,0) = 2\xi\sqrt{1-\xi^2} = \dfrac{1}{R_{\mathrm{d,max}}(\xi)}$
$TR_{\max} = 1$	$R_{\max} = 1$

Fig. A.10. Dynamic amplification factor R for $\xi = 0.1$ (*thick black curve*) with the location of β_1 (*red dots*) and β_2 (*blue dots*) for some δ_0 values (*horizontal dashed lines*) [41]. For $\beta_1 < \beta < \beta_2$ (*thick horizontal yellow lines*) impact surely occurs for geometric reasons. (For interpretation of the references to color in this figure legend, the reader is referred to the web version of this article.)

denoted as β_1 and β_2 respectively (with $\beta_1 < \beta_2$), can be determined analytically by solving, for each $\xi - \delta_0$ pair, the equation $R(\xi,\beta) = \delta_0$, that is by finding the intersections between the curve representative of the displacement amplification factor $R(\xi,\beta)$, corresponding to the selected ξ value, and the horizontal line $\delta_0 = constant$, as shown in Fig. A.10 for $\xi = 0.1$.

In this figure, β_1 and β_2 are represented with red and blue dots respectively, for some δ_0 values, and the frequency interval $\beta_1 \leq \beta \leq \beta_2$ is highlighted with horizontal yellow lines. The roots of equation $R(\xi,\beta) = \delta_0$ (Table A.1) have the following expressions:

• for $0 < \xi < \sqrt{2}/2$:

$$\begin{cases} \beta_1(\xi,\delta_0) = \sqrt{1-2\xi^2 - \dfrac{2\xi}{\delta_0}\sqrt{(\delta_0^2-1)(\xi^2-1)}} \\[4mm] \beta_2(\xi,\delta_0) = \sqrt{1-2\xi^2 + \dfrac{2\xi}{\delta_0}\sqrt{(\delta_0^2-1)(\xi^2-1)}} \end{cases}$$

(A.1)

• for $\sqrt{2}/2 \leq \xi < 1$:

$$\begin{cases} \beta_1(\xi,\delta_0) = \sqrt{1-2\xi^2 - \dfrac{1}{\delta_0}\sqrt{1+(2\xi\delta_0)^2(\xi^2-1)}} \\[4mm] \beta_2(\xi,\delta_0) = \sqrt{1-2\xi^2 + \dfrac{1}{\delta_0}\sqrt{1+(2\xi\delta_0)^2(\xi^2-1)}} \end{cases}$$

(A.2)

From Fig. A.10, taken from [41], it can be observed that, for a given ξ value (i.e. $\xi = 0.1$), different situations may occur depending on the dimensionless gap δ_0. For $\delta_0 = 1$, that is in free flight condition, the two roots coincide ($\beta_1 = \beta_2 = \beta_{\mathrm{Rd}}$) and thus impact never occurs for any β value.

Appendix B. Dissipated energy

Dimensionless energy balance equations

Integrating the dimensionless equations of motion Eqs. (6a) and (6b) with respect to q ($\mathrm{d}q = q'\mathrm{d}\tau$) yields the mass contribution when the bumper j is contact and the bumper i is detached:

$$\int_{\tau_i}^{\tau_o} q''(\tau)q'(\tau)\mathrm{d}\tau + 2\xi\int_{\tau_i}^{\tau_o} q'(\tau)^2\mathrm{d}\tau + \int_{\tau_i}^{\tau_o} q(\tau)q'(\tau)\mathrm{d}\tau + \int_{\tau_i}^{\tau_o} f_j(\tau)\cdot\psi_1\left[\delta_j(\tau)\right]\cdot\psi_2\left[f_j(\tau)\right]q'(\tau)\mathrm{d}\tau = -a_{\mathrm{G}}\int_{\tau_i}^{\tau_o}\sin\beta\tau q'(\tau)\mathrm{d}\tau$$
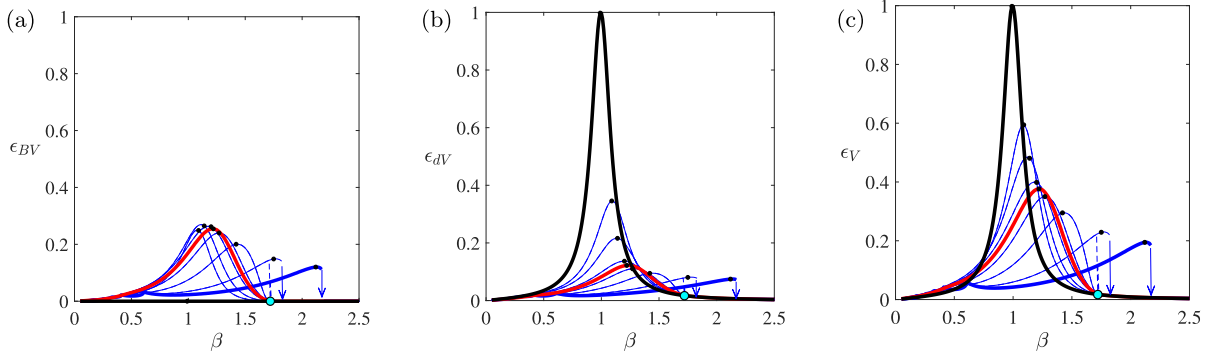
(B.1)

Fig. B.11. Sections of the PRCs of the dimensionless energy dissipated by: (a) both bumpers (ϵ_{BV}), (b) damper (ϵ_{dV}) and (c) system (ϵ_V) in one cycle for $\xi = 0.1$, $\delta_0 = 0.1$ and $\gamma = 4$ as λ varies. Each curve corresponds to a different value of the stiffness ratio λ: red PRC refers to the optimal case, black PRC refers to the case of free flight without bumpers (only damper, $\delta_0 \geq 1$). (For interpretation of the references to color in this figure legend, the reader is referred to the web version of this article.)
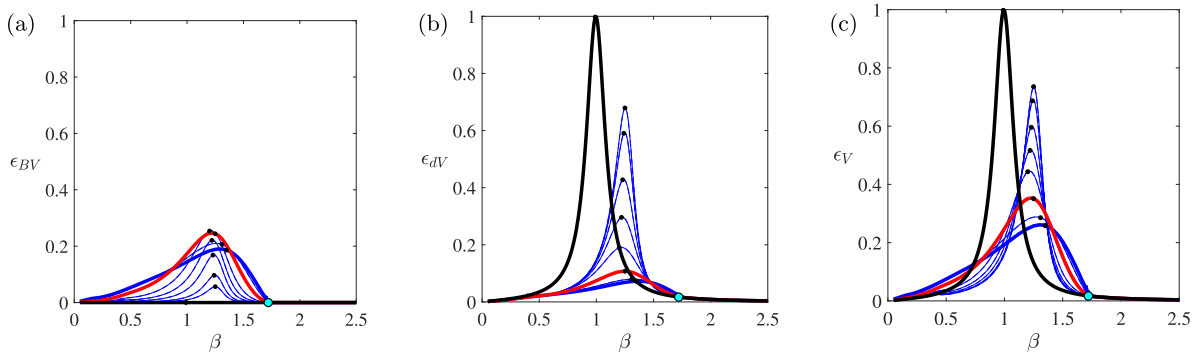

Fig. B.12. Sections of the PRCs of the dimensionless energy dissipated by: (a) both bumpers (ϵ_{BV}), (b) damper (ϵ_{dV}) and (c) system (ϵ_V) in one cycle for $\xi = 0.1$, $\delta_0 = 0.1$ and $\lambda = 0.7$ as γ varies. Each curve corresponds to a different value of the stiffness ratio γ: red PRC refers to the optimal case, black PRC refers to the case of free flight without bumpers (only damper, $\delta_0 \geq 1$). (For interpretation of the references to color in this figure legend, the reader is referred to the web version of this article.)

the contribution of the detached bumper i:

$$\int_{\tau_i}^{\tau_o} f_i(\tau)q'(\tau)\mathrm{d}\tau = 0 \tag{B.2}$$

as well as the contribution of bumper j in the phase of contact:

$$\int_{\tau_i}^{\tau_o} f_j(\tau) \cdot \psi_1\left[\delta_j(\tau)\right] \cdot \psi_2\left[f_j(\tau)\right] q'(\tau)\mathrm{d}\tau = 2\xi\gamma_j \int_{\tau_i}^{\tau_o} q_j'(\tau)q'(\tau)\mathrm{d}\tau + \lambda_j \int_{\tau_i}^{\tau_o} q_j(\tau)q'(\tau)\mathrm{d}\tau \tag{B.3}$$

In particular, the energy dissipated by the damper is:

$$e_{dV} = 2\xi \int_{\tau_i}^{\tau_o} q'(\tau)^2 \mathrm{d}\tau \tag{B.4}$$

while the energy dissipated by the jth ($j = $ R, L) bumper is:

$$e_{jV} = 2\xi\gamma_j \int_{\tau_i}^{\tau_o} q_j'(\tau)q'(\tau)\mathrm{d}\tau \tag{B.5}$$

Normalization

The dimensionless contributions to the energy dissipated in a steady state cycle are then normalized with respect to e_{dV0}, which is the maximum (dimensionless) energy dissipated in one cycle from the damper alone at the free flight resonance:

$$\text{Damper}: \epsilon_{dV} = \frac{e_{dV}}{e_{dV0}} \tag{B.6a}$$

$$\text{Bumpers}: \quad \epsilon_{BV} = \frac{e_{BV}}{e_{dV0}} \tag{B.6b}$$

$$\text{System}: \quad \epsilon_V = \frac{e_V}{e_{dV0}} \tag{B.6c}$$

where $e_{BV} = e_{RV} + e_{LV}$ is the energy dissipated by both bumpers and $e_V = e_{dV} + e_{BV}$.

Illustration

The contributions to the dissipated energy are then illustrated in the following graphs which were drawn using the same data used in Fig. 4. The meaning of the colors is the same as in Fig. 4.

Appendix C. Nomenclature

For reader's convenience, the following Table C.2 summarizes the meaning of the dimensionless response quantities and mechanical parameters of the bumpers (stiffness and damping) cited in Sections 3–5.

Table C.2
List of symbols.

Symbol	Description
η_i	response's excursion (i = a, d, F, B)
η_i^*	value of the response's excursion at the primary resonance (i = a, d, F, B)
$\eta_{d,st}$	excursion of the static displacement of the mass
β_R	absolute acceleration's resonant frequency
$\eta_{a,MIN}^*$	absolute minimum of the peak acceleration for $\xi = constant$ and $\delta_0 = constant$
$\tilde{\eta}_a^*$	normalized excursion of the absolute acceleration of the mass
$\eta_i\|_{\beta=0}$	value of the response's excursion for $\beta = 0$ (i = a, d)
$\lambda_{MIN} - \gamma_{MIN}$	$\lambda - \gamma$ pair corresponding to the absolute minimum of the peak acceleration for $\lambda = constant$ and γ freely varying within suitable ranges (free optimal design, free optimization, not constrained by the optimality condition)
$\lambda_{opt} - \gamma_{opt}$	$\lambda - \gamma$ pair corresponding to the absolute minimum of the peak acceleration for $\gamma = constant$ and $\lambda = constant$ respectively (constrained optimal design, constrained optimization, not constrained by the optimality condition)
$\tilde{\lambda} - \tilde{\gamma}$	normalized stiffness and damping ratios
$\lambda_{opt}^* - \gamma_{opt}^*$	$\lambda - \gamma$ pair corresponding to the minimum peak value of the acceleration constrained by the optimality condition (Eq. (1))
$\lambda_{opt}^*(A) - \gamma_{opt}^*(A)$	$= \lambda_{opt}^* - \gamma_{opt}^*$
$\lambda_{opt}^*(MO) - \gamma_{opt}^*(MO)$	$\lambda - \gamma$ pair corresponding to the multi-objective optimization, constrained by the optimality condition

References

[1] E. Renzi, M. De Angelis, Optimal semi-active control and non-linear dynamic response of variable stiffness structures, J. Vib. Control 11 (10) (2005) 1253–1289, http://dx.doi.org/10.1177/1077546305054597.

[2] P. Komodromos, P.C. Polycarpou, L. Papaloizou, M.C. Phocas, Response of seismically isolated buildings considering poundings, Earthq. Eng. Struct. Dyn. 36 (2007) 1605–1622, http://dx.doi.org/10.1002/eqe.692Response.

[3] P.C. Polycarpou, P. Komodromos, On poundings of a seismically isolated building with adjacent structures during strong earthquakes, Earthq. Eng. Struct. Dyn. 39 (2010) 933–940, http://dx.doi.org/10.1002/eqe.975.

[4] P.C. Polycarpou, P. Komodromos, Numerical investigation of potential mitigation measures for poundings of seismically isolated buildings, Earthq. Struct. 2 (1) (2011) 1–24, http://dx.doi.org/10.12989/eas.2011.2.1.001.

[5] S.A. Anagnostopoulos, Pounding of buildings in series during earthquakes, Earthq. Eng. Struct. Dyn. 16 (3) (1988) 443–456, http://dx.doi.org/10.1002/eqe.4290160311.

[6] M. Papadrakakis, H.P. Mouzakis, Earthquake simulator testing of pounding between adjacent buildings, Earthq. Eng. Struct. Dyn. 24 (6) (1995) 811–834, http://dx.doi.org/10.1002/eqe.4290240604.

[7] A. Masroor, G. Mosqueda, Experimental simulation of base-isolated buildings pounding against moat wall and effects on superstructure response, Earthq. Eng. Struct. Dyn. 41 (14) (2012) 2093–2109, http://dx.doi.org/10.1002/eqe.2177.

[8] P.C. Polycarpou, P. Komodromos, A.C. Polycarpou, A nonlinear impact model for simulating the use of rubber shock absorbers for mitigating the effects of structural pounding during earthquakes, Earthq. Eng. Struct. Dyn. 42 (1) (2013) 81–100, http://dx.doi.org/10.1002/eqe.2194.

[9] V. Crozet, I. Politopoulos, M. Yang, J.M. Martinez, S. Erlicher, Sensitivity analysis of pounding between adjacent structures, Earthq. Eng. Struct. Dyn. 47 (1) (2018) 219–235, http://dx.doi.org/10.1002/eqe.2949.

[10] A.S. Whittaker, M. Kumar, M. Kumar, Seismic isolation of nuclear power plants, Nucl. Eng. Technol. 46 (5) (2014) 569–580, http://dx.doi.org/10.5516/NET.09.2014.715.

[11] F. Peterka, Bifurcations and transition phenomena in an impact oscillator, Chaos Solitons Fractals 7 (10 SPEC. ISS.) (1996) 1635–1647, http://dx.doi.org/10.1016/S0960-0779(96)00028-8.

[12] P.J. Christopher, B. Dobson, N.A. Alexander, Exploring the dynamics of base-excited structures impacting a rigid stop, Math. Probl. Eng. 2020 (2020) http://dx.doi.org/10.1155/2020/6721025.

[13] D. Costa, V. Vaziri, M. Kapitaniak, S. Kovacs, E. Pavlovskaia, M.A. Savi, M. Wiercigroch, Chaos in impact oscillators not in vain: Dynamics of new mass excited oscillator, Nonlinear Dynam. (2020) http://dx.doi.org/10.1007/s11071-020-05644-0.

[14] M. Wiercigroch, S. Kovacs, S. Zhong, D. Costa, V. Vaziri, M. Kapitaniak, E. Pavlovskaia, Versatile mass excited impact oscillator, Nonlinear Dynam. 99 (1) (2020) 323–339, http://dx.doi.org/10.1007/s11071-019-05368-w.

[15] H. Gritli, S. Belghith, Diversity in the nonlinear dynamic behavior of a one-degree-of-freedom impact mechanical oscillator under OGY-based state-feedback control law: Order, chaos and exhibition of the border-collision bifurcation, Mech. Mach. Theory 124 (2018) 1–41, http://dx.doi.org/10.1016/j.mechmachtheory.2018.02.001.

[16] J. Ing, E. Pavlovskaia, M. Wiercigroch, Dynamics of a nearly symmetrical piecewise linear oscillator close to grazing incidence: Modelling and experimental verification, Nonlinear Dynam. 46 (3) (2006) 225–238, http://dx.doi.org/10.1007/s11071-006-9045-9.

[17] M. Wiercigroch, V.W. Sin, Experimental study of a symmetrical plecewlse base-excited oscillator, J. Appl. Mech. Trans. ASME 65 (3) (1998) 657–663, http://dx.doi.org/10.1115/1.2789108.

[18] G. Luo, L. Ma, X. Lv, Dynamic analysis and suppressing chaotic impacts of a two-degree-of-freedom oscillator with a clearance, Nonlinear Anal. RWA 10 (2) (2009) 756–778, http://dx.doi.org/10.1016/j.nonrwa.2007.11.002.

[19] G.W. Luo, X.H. Lv, Y.Q. Shi, Vibro-impact dynamics of a two-degree-of freedom periodically-forced system with a clearance: Diversity and parameter matching of periodic-impact motions, Int. J. Non Linear. Mech. 65 (2014) 173–195, http://dx.doi.org/10.1016/j.ijnonlinmec.2014.04.013.

[20] X. Lyu, Q. Gao, G. Luo, Dynamic characteristics of a mechanical impact oscillator with a clearance, Int. J. Mech. Sci. 178 (2020) 105605, http://dx.doi.org/10.1016/j.ijmecsci.2020.105605.

[21] S. Yin, G. Wen, J. Ji, H. Xu, Novel two-parameter dynamics of impact oscillators near degenerate grazing points, Int. J. Non Linear. Mech. 120 (2020) 103403, http://dx.doi.org/10.1016/j.ijnonlinmec.2020.103403.

[22] L. Wang, W. Xu, Y. Li, Impulsive control of a class of vibro-impact systems, Phys. Lett. Sect. A Gen. At. Solid State Phys. 372 (32) (2008) 5309–5313, http://dx.doi.org/10.1016/j.physleta.2008.06.027.

[23] S. Lenci, G. Rega, A procedure for reducing the Chaotic Response Region in an impact mechanical system, Nonlinear Dynam. 15 (4) (1998) 391–409, http://dx.doi.org/10.1023/A:1008209513877.

[24] Y. Liu, J. Páez Chávez, Controlling multistability in a vibro-impact capsule system, Nonlinear Dynam. 88 (2) (2017) 1289–1304, http://dx.doi.org/10.1007/s11071-016-3310-3.

[25] Y. Liu, M. Wiercigroch, E. Pavlovskaia, Z. Peng, Forward and backward motion control of a vibro-impact capsule system, Int. J. Non Linear. Mech. 70 (2015) 30–46, http://dx.doi.org/10.1016/j.ijnonlinmec.2014.10.009.

[26] H. Gritli, Robust master-slave synchronization of chaos in a one-sided 1-DoF impact mechanical oscillator subject to parametric uncertainties and disturbances, Mech. Mach. Theory 142 (2019) http://dx.doi.org/10.1016/j.mechmachtheory.2019.103610.

[27] F. Turki, H. Gritli, S. Belghith, Robust position control of a two-sided 1-dof impacting mechanical oscillator subject to an external persistent disturbance by means of a state-feedback controller, Complexity 2019 (2019) 18–22, http://dx.doi.org/10.1155/2019/9174284.

[28] F. Turki, H. Gritli, S. Belghith, An LMI-based design of a robust state-feedback control for the master-slave tracking of an impact mechanical oscillator with double-side rigid constraints and subject to bounded-parametric uncertainty, Commun. Nonlinear Sci. Numer. Simul. 82 (2020) 1–26, http://dx.doi.org/10.1016/j.cnsns.2019.105020.

[29] P. Brzeski, E. Pavlovskaia, T. Kapitaniak, P. Perlikowski, Controlling multistability in coupled systems with soft impacts, Int. J. Mech. Sci. 127 (2017) 118–129, http://dx.doi.org/10.1016/j.ijmecsci.2016.12.022.

[30] X. Sun, H. Zhang, W. Meng, R. Zhang, K. Li, T. Peng, Primary resonance analysis and vibration suppression for the harmonically excited nonlinear suspension system using a pair of symmetric viscoelastic buffers, Nonlinear Dynam. 94 (2) (2018) 1243–1265, http://dx.doi.org/10.1007/s11071-018-4421-9.

[31] Z. Hao, Q. Cao, M. Wiercigroch, Two-sided damping constraint control strategy for high-performance vibration isolation and end-stop impact protection, Nonlinear Dynam. 86 (4) (2016) 2129–2144, http://dx.doi.org/10.1007/s11071-016-2685-5.

[32] Z. Hao, Q. Cao, The isolation characteristics of an archetypal dynamical model with stable-quasi-zero-stiffness, J. Sound Vib. 340 (2015) 61–79, http://dx.doi.org/10.1016/j.jsv.2014.11.038.

[33] L.Y. Lu, G.L. Lin, Predictive control of smart isolation system for precision equipment subjected to near-fault earthquakes, Eng. Struct. 30 (11) (2008) 3045–3064, http://dx.doi.org/10.1016/j.engstruct.2008.04.016.

[34] A. Reggio, M. De Angelis, Optimal design of an equipment isolation system with nonlinear hysteretic behavior, Earthq. Eng. Struct. Dyn. 42 (2013) 1907–1930, http://dx.doi.org/10.1002/eqe.2304.

[35] A. Reggio, M. De Angelis, Combined primary-secondary system approach to the design of an equipment isolation system with High-Damping Rubber Bearings, J. Sound Vib. 333 (9) (2014) 2386–2403, http://dx.doi.org/10.1016/j.jsv.2013.12.006.

[36] I. Caliò, M. Marletta, Passive control of the seismic rocking response of art objects, Eng. Struct. 25 (8) (2003) 1009–1018, http://dx.doi.org/10.1016/S0141-0296(03)00045-2.

[37] A. Contento, A. Di Egidio, Investigations into the benefits of base isolation for non-symmetric rigid blocks, Earthq. Eng. Struct. Dyn. 38 (2009) 849–866, http://dx.doi.org/10.1002/eqe.870.

[38] S. Sorace, G. Terenzi, Seismic performance assessment and base-isolated floor protection of statues exhibited in museum halls, Bull. Earthq. Eng. 13 (6) (2015) 1873–1892, http://dx.doi.org/10.1007/s10518-014-9680-3.

[39] E.A. Mavronicola, P.C. Polycarpou, P. Komodromos, Effect of planar impact modeling on the pounding response of base-isolated buildings, Front. Built Environ. 2 (11) (2016) 1–16, http://dx.doi.org/10.3389/fbuil.2016.00011.

[40] U. Andreaus, M. De Angelis, Influence of the characteristics of isolation and mitigation devices on the response of single-degree-of-freedom vibro-impact systems with two-sided bumpers and gaps via shaking table tests, Struct. Control Health Monit. 27 (5) (2020) 1–21, http://dx.doi.org/10.1002/stc.2517.

[41] G. Stefani, M. De Angelis, U. Andreaus, The effect of the presence of obstacles on the dynamic response of single-degree-of-freedom systems: Study of the scenarios aimed at vibration control, J. Sound Vib. 531 (2022) 116949, http://dx.doi.org/10.1016/j.jsv.2022.116949.

[42] U. Andreaus, M. De Angelis, Nonlinear dynamic response of a base-excited SDOF oscillator with double-side unilateral constraints, Nonlinear Dynam. 84 (3) (2016) 1447–1467, http://dx.doi.org/10.1007/s11071-015-2581-4.

[43] U. Andreaus, P. Baragatti, M. De Angelis, S. Perno, A preliminary experimental study about two-sided impacting SDOF oscillator under harmonic excitation, J. Comput. Nonlinear Dyn. 12 (6) (2017) 061010, http://dx.doi.org/10.1115/1.4036816.

[44] U. Andreaus, P. Baragatti, M. De Angelis, S. Perno, Shaking table tests and numerical investigation of two-sided damping constraint for end-stop impact protection, Nonlinear Dynam. 90 (4) (2017) 2387–2421, http://dx.doi.org/10.1007/s11071-017-3810-9.

[45] U. Andreaus, M. De Angelis, Experimental and numerical dynamic response of a SDOF vibro-impact system with double gaps and bumpers under harmonic excitation, Int. J. Dyn. Control 7 (4) (2019) 1278–1292, http://dx.doi.org/10.1007/s40435-019-00532-x.

[46] G. Stefani, M. De Angelis, U. Andreaus, Numerical study on the response scenarios in a vibro-impact single-degree-of-freedom oscillator with two unilateral dissipative and deformable constraints, Commun. Nonlinear Sci. Numer. Simul. 99 (2021) 105818, http://dx.doi.org/10.1016/j.cnsns.2021.105818.

[47] G. Stefani, M. De Angelis, U. Andreaus, Influence of the gap size on the response of a single-degree-of-freedom vibro-impact system with two-sided constraints: experimental tests and numerical modeling, Int. J. Mech. Sci. 206 (2021) 106617, http://dx.doi.org/10.1016/j.ijmecsci.2021.106617.

[48] K.J. Bathe, Finite Element Procedures, Prentice-Hall, Englewood Cliffs New Jersey, New York, 1996, p. 1037.

[49] M. Machado, P. Moreira, P. Flores, H.M. Lankarani, Compliant contact force models in multibody dynamics: Evolution of the hertz contact theory, Mech. Mach. Theory 53 (2012) 99–121, http://dx.doi.org/10.1016/j.mechmachtheory.2012.02.010.

[50] L. Skrinjar, J. Slavi, A review of continuous contact-force models in multibody dynamics, Int. J. Mech. Sci. 145 (2018) 171–187, http://dx.doi.org/10.1016/j.ijmecsci.2018.07.010.

[51] P. Flores, M. Machado, M.T. Silva, J.M. Martins, On the continuous contact force models for soft materials in multibody dynamics, Multibody Syst. Dyn. 25 (2011) 357–375, http://dx.doi.org/10.1007/s11044-010-9237-4.

[52] P. Flores, H.M. Lankarani, Contact Force Models for Multibody Dynamics, Springer, 2016.

[53] Z. Qu, S. Kishiki, T. Nakazawa, Influence of isolation gap size on the collapse performance of seismically base-isolated buildings, Earthq. Spectra 29 (4) (2013) 1477–1494, http://dx.doi.org/10.1193/031912EQS097M.

[54] Y. Bao, T.C. Becker, Inelastic response of base-isolated structures subjected to impact, Eng. Struct. 171 (2018) 86–93, http://dx.doi.org/10.1016/j.engstruct.2018.05.091.

[55] R. Jankowski, K. Wilde, Y. Fujino, Reduction of pounding effects in elevated bridges during earthquakes, Earthq. Eng. Struct. Dyn. 29 (2) (2000) 195–212, http://dx.doi.org/10.1002/(SICI)1096-9845(200002)29:2<195::AID-EQE897>3.0.CO;2-3.

[56] S.E. Abdel Raheem, Pounding mitigation and unseating prevention at expansion joints of isolated multi-span bridges, Eng. Struct. 31 (10) (2009) 2345–2356, http://dx.doi.org/10.1016/j.engstruct.2009.05.010.

[57] M. Dicleli, S. Buddaram, Comprehensive evaluation of equivalent linear analysis method for seismic-isolated structures represented by SDOF systems, Eng. Struct. 29 (8) (2007) 1653–1663.

[58] P.J. Sayani, K.L. Ryan, Evaluation of approaches to characterize seismic isolation systems for design, J. Earthquake Eng. 13 (6) (2009) 835–851.

[59] S. Bhagat, A.C. Wijeyewickrema, Seismic response evaluation of base-isolated reinforced concrete buildings under bidirectional excitation, Earthq. Eng. Eng. Vib. 16 (2) (2017) 365–382.

[60] T. Taniguchi, A. Der Kiureghian, M. Melkumyan, Effect of tuned mass damper on displacement demand of base-isolated structures, Eng. Struct. 30 (12) (2008) 3478–3488.

[61] N. Hoang, Y. Fujino, P. Warnitchai, Optimal tuned mass damper for seismic applications and practical design formulas, Eng. Struct. 30 (3) (2008) 707–715.

[62] M. De Angelis, R. Giannini, F. Paolacci, Experimental investigation on the seismic response of a steel liquid storage tank equipped with floating roof by shaking table tests, Earthq. Eng. Struct. Dyn. 39 (4) (2010) 377–396, http://dx.doi.org/10.1002/eqe.945.

[63] F. Paolacci, R. Giannini, M. De Angelis, Seismic response mitigation of chemical plant components by passive control techniques, J. Loss Prev. Process Ind. 26 (5) (2013) 924–935.

[64] A.K. Chopra, Dynamic of Structures: Theory and Applications To Earthquake Engineering, fourth ed., Pearson, Englewood Cliffs, New Jersey, 2012,